Applied Surface Science 726 (2026) 165927

Contents lists available at ScienceDirect

Applied Surface Science

journal homepage: www.elsevier.com/locate/apsusc

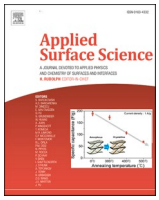

Full Length Article

Adhesion forces between AFM tips and TiO_2 nanoparticles to investigate the formation of natural coatings

Narjes Tayyebi Sabet Khomami [a,*], Allan Philippe [a,*], Abd Alaziz Abu Quba [a], Michel Gad [b], Oliver Lechtenfeld [b], Fintan Hahn [a], Vanessa Trouillet [c], Jean-Michel Guigner [d]

[a] iES Landau, Institute for Environmental Sciences, Group of Environmental and Soil Chemistry, University of Kaiserslautern-Landau (RPTU), 76829 Landau, Germany
[b] Department of Environmental Analytical Chemistry, Helmholtz Centre for Environmental Research – UFZ, 04318 Leipzig, Germany
[c] Karlsruhe Nano Micro Facility (KNMFi) and Institute for Applied Materials (IAM-ESS), Karlsruhe Institute of Technology (KIT), 76344 Karlsruhe, Germany
[d] IMPMC, Sorbonne University, CNRS – UMR 7590, MNHN, Paris, France

ARTICLE INFO

Keywords:
AFM
Adhesion forces
Nanoparticles
Coating
Surface waters
Eco-corona

ABSTRACT

When nanoparticles enter aquatic environments, they acquire natural surface coatings (eco-coronas) that govern their fate, transport, and toxicity. This study employs atomic force microscopy (AFM) adhesion force mapping to characterize these coatings following in situ formation under natural conditions. Titanium dioxide nanoparticles (n-TiO_2) and flat single-crystal TiO_2 substrates (absence of curvature and roughness effects) were exposed to three chemically distinct surface waters, revealing pronounced variability in adhesion force strength, range (min–max differences), and spatial patchiness, nanoscale heterogeneity metrics inaccessible to bulk techniques.

Moran's I analysis of crystal-TiO_2 confirmed positive spatial autocorrelation across samples, indicating patchy eco-coronas. Terrestrially dominated water (high DOC, humic-rich) produced the widest adhesion ranges, reflecting polydisperse humic adsorption. Microbial-enriched waters exhibited high adhesion forces comparable to terrestrial waters but lower variability ranges, while calcareous water (high Ca^{2+}, ionic strength) yielded the lowest forces with less ordered spatial patterns. Moreover, sessile drop contact angle measurements on crystals further revealed macroscopic hydrophilicity changes.

In addition, complementary analyses of particle size, morphology, surface charge, and functional groups of the exposed nanoparticles to the surface waters provided multi-technique validation of surface modifications. These results establish AFM adhesion mapping as a powerful approach for resolving eco-corona heterogeneity under environmentally relevant conditions.

1. Introduction

Titanium dioxide nanoparticles (n-TiO_2) are utilized in a wide range of industries and consumer products, including food, cosmetics, paint, construction, wastewater treatment, catalysis, and the biomedical sector [1–3]. The n-TiO_2 market size is projected to reach $20 billion by 2025 [4]. Extensive production and widespread application have led to the inevitable release of n-TiO_2 into aquatic environments [5]. Around the early 2010 s, concerns emerged regarding the potential environmental and health risks associated with n-TiO_2, including adverse effects on aquatic life such as fish, invertebrates, and microbial communities [6–8]. Since then, environmental scientists have focused on understanding the probable transformations of these particles in natural waters [9,10]. Once nanoparticles enter aquatic environments, they can interact with organic and inorganic substances, such as dissolved organic matter (DOM) or dissolved salts, leading to the formation of natural coatings on their surfaces [11]. Several studies have demonstrated that organic coatings can substantially alter the behavior of n-TiO_2. Auffan et al. [12] showed that polydimethylsiloxane coatings rapidly desorb and oxidize in aqueous media, indicating that surface layers are unstable under environmental conditions. Bing et al. [13] reported that protein coronas affect nanoparticle size, surface charge, and protein secondary structure, while Du et al. [14] found that corona formation depends on the crystalline phase of TiO_2. Furthermore, Yuan et al. [15] emphasized the role of hydrogen bonding, showing that corona mass increases with higher surface hydroxyl density. Collectively, these studies illustrate the diverse chemical mechanisms that govern corona formation on n-TiO_2.

* Corresponding authors.
E-mail addresses: n.tayyebi@rptu.de (N. Tayyebi Sabet Khomami), a.philippe@rptu.de (A. Philippe).

https://doi.org/10.1016/j.apsusc.2026.165927
Received 5 August 2025; Received in revised form 19 December 2025; Accepted 12 January 2026
Available online 13 January 2026

Over the past few decades, AFM has become a powerful tool for studying the formation and properties of coatings on nanoparticles [16,17]. AFM is a high-resolution imaging technique that enables the investigation of surface topography and physicochemical properties of solid surfaces. The sample is scanned using a tip mounted on a spring-like cantilever [18]. In AFM adhesion force measurements, the force between the tip and the sample is monitored during scanning by measuring the deflection of the cantilever, which is then converted into force-distance curves [19]. For instance, protein-surface adhesion to mesoporous TiO_2 is shown to strengthen with larger pore sizes and increased surface roughness, primarily due to greater contact area between the protein and TiO_2 surface [20]. AFM adhesion measurements have also been applied in environmental studies, such as evaluating soil properties by investigating bacterial adhesion to mineral surfaces [21]. They have also been used to explore the interactions of natural organic matter (NOM) with mica surfaces, demonstrating that these interactions depend not only on the characteristics of NOM, such as functional groups, but also on the ionic strength of the reaction medium [22]. Regarding coating formation on nanoparticles, Oras et al. [23] investigated the adhesion forces between gold nanoparticles functionalized with various hydrophilic and hydrophobic groups and silicon tips, showing substantial differences depending on the nature of these terminal functional groups.

Although numerous studies have characterized natural coating formation on nanoparticles under controlled laboratory conditions [24–27], their direct applicability to complex aquatic environments remains uncertain. Louie et al. reviewed how macromolecular coatings affect key physicochemical processes influencing nanomaterial fate in the environment. They identified the main research gap as insufficient characterization of these adsorbed layers and their changes in natural systems [28]. Laboratory models simplify the complexity of natural waters, potentially overlooking heterogeneous and dynamic interactions that drive eco-corona formation, the evolving layer of natural organic matter and inorganic ions adsorbing onto particle surfaces during environmental exposure. For instance, inorganic ion effects cannot be disentangled from DOM sorption due to complex, dynamic interactions between ions and organic molecules, such as cation bridging that forms intermolecular assemblies. This discrepancy highlights a critical gap in understanding the evolution of nanoparticle surface properties under truly natural conditions.

To address the abovementioned challenge, passive sampling strategies have gained increasing attention because they allow surfaces or particles to interact with their surrounding environment without active manipulation, thereby minimizing artefacts introduced during sample handling. AFM substrates exposed in natural or urban settings have revealed nano to millimeter-scale films consisting of mineral particles, organic matter, and biological macromolecules [29]. Additional AFM-based investigations have examined the passive growth of surface films on stainless steel in aqueous conditions, utilizing gold markers as reference points [30]. Moreover, studies have shown that AFM can characterize atmospheric aerosol particles with minimal sample preparation [31].

Building on this concept, we previously developed a method using dialysis bags to investigate the in situ formation of nanoparticle coatings in natural waters [32]. The semipermeable membrane permits the diffusion of dissolved organic matter and ions, enabling eco-corona formation under authentic environmental conditions while avoiding the mixing with natural colloids. This refinement was not implemented in previous passive sampling methods. By eliminating interference from suspended colloids, the system allows a more targeted investigation of DOM-ion-nanoparticle interactions. Using this approach, we combined analytical techniques and complementary statistical analyses to characterize the chemical composition and variability of coatings formed inside dialysis bags, for instance, Philippe et al. [33] have reported the use of the dialysis bag approach applied to a wide variety of surface waters to predict the zeta potential of nanoparticles with a realistic eco-corona and explore the coating composition using XPS. However, this study focused on bulk properties without information on the heterogeneity of the coating at the nanoparticle scale.

In the present study, this methodology is extended by employing AFM-based adhesion force measurements to gain deeper insight into the structure and heterogeneity of the eco-corona (Fig. 1). This study demonstrates the potential of AFM adhesion force mapping as a powerful tool for characterizing nanoparticle coatings formed under natural environmental conditions. The primary objective is to evaluate whether adhesion forces serve as sensitive indicators of eco-corona physicochemical properties. As a feasibility study, this work focuses on assessing the method's potential and the nature of obtainable nanoscale information. We hypothesize that adhesion force variations reflect differences in eco-corona composition and structural organization, thereby providing nanoscale insights into its heterogeneity.

The novelty of this work lies in combining realistic environmental exposure with nanoscale characterization, demonstrating that passive sampling via dialysis bags provides a simple, low-cost, and broadly applicable method for studying eco-corona formation across diverse freshwater systems. A central methodological challenge in applying AFM to such systems lies in immobilizing nanoparticles without altering their naturally formed coatings. To address this, we developed an immobilization procedure that preserves individual particles under natural conditions, bypassing the need for conventional sample preparation after coating formation and thereby minimizing perturbations during handling (Fig. 1A). To the best of our knowledge, this approach has not been used previously in coating studies of nanoparticles.

We compared adhesion forces across three different surface waters selected to represent extreme differences in ionic strength and DOM. We further examined edge effects, quantified roughness contributions by including flat crystal-TiO_2 surfaces as references [34], and discussed the implications of patchy surface coverage. Additionally, we used the flat crystal-TiO_2 surfaces to investigate the relationship between hydrophilicity (water contact angle) and AFM measurements, as using flat crystal-TiO_2 avoids complications associated with the small and irregular geometries of n-TiO_2, such as air pocket formation and sample heterogeneity [35]. AFM adhesion force mapping revealed variability in adhesion force strength, range (min–max differences), and spatial patchiness, key indicators of exposed surface water chemistry. Complementary techniques (Fig. 1B), including high-resolution transmission electron microscopy (HR-TEM), zeta potential (ζ-potential), attenuated total reflectance Fourier transform infrared spectroscopy (ATR-FTIR), X-ray photoelectron spectroscopy (XPS), and laser desorption/ionization Fourier transform ion cyclotron resonance mass spectrometry (LDI-FT-ICR MS), comprehensively characterized the chemical and structural features of these natural coatings.

This work provides a basis for extending AFM-based characterization to larger and more environmentally diverse sample sets. With an increased number of surface-water exposures, statistical analyses can be conducted to elucidate patterns governing sorption processes within the eco-corona. When integrated with complementary analytical techniques, these datasets have the potential to yield more comprehensive information on eco-corona composition and formation mechanisms. Moreover, as n-TiO_2 P25 consists predominantly of anatase-phase TiO_2, future studies can expand this approach to nanoparticles with different crystal phases to assess how phase-dependent surface properties influence eco-corona formation.

2. Materials and methods

2.1. Materials

2.1.1. n-TiO_2

Aeroxide® n-TiO_2 P25 powder (Evonik Degussa, Germany) is a commercially available titanium dioxide reference material consisting of approximately 80 % anatase and 20 % rutile. This hydrophilic

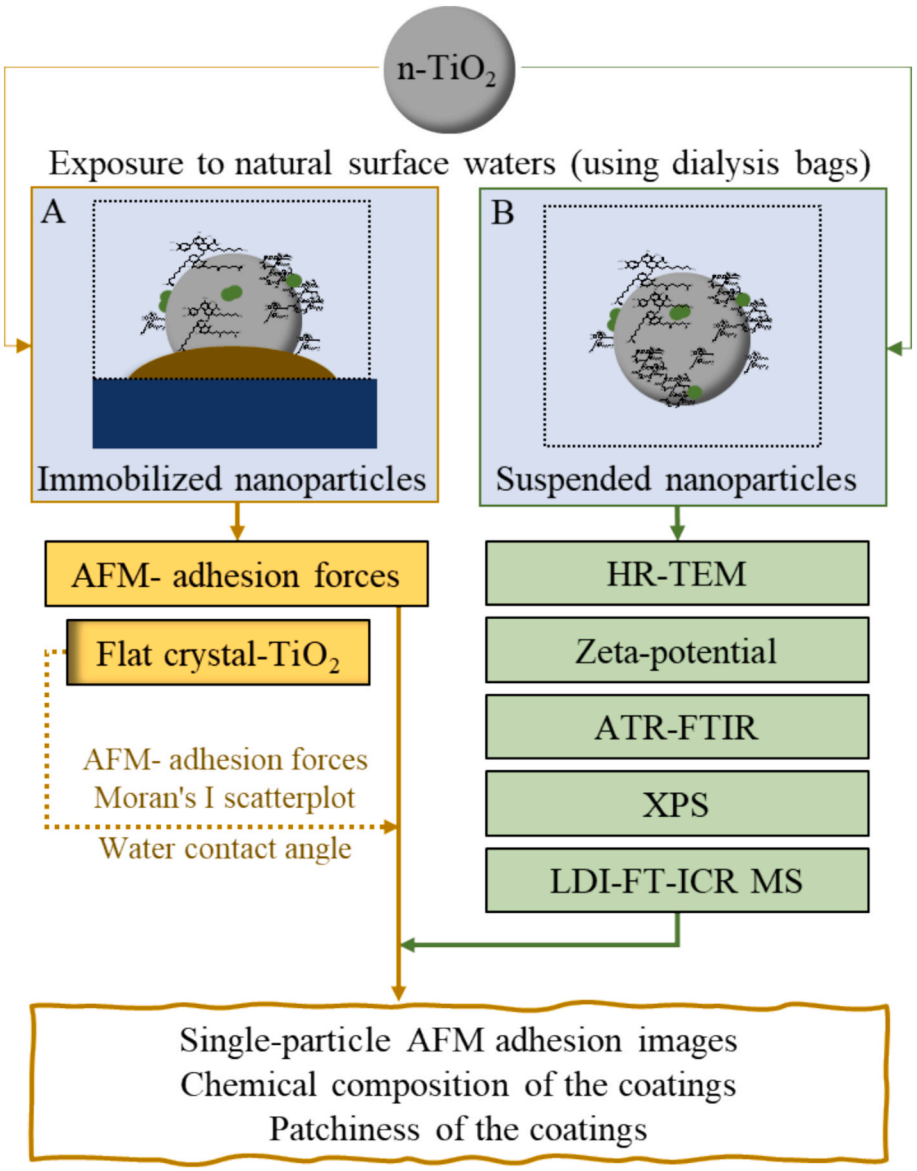

Fig. 1. Schematic overview of the study. n-TiO_2 were exposed to three surface waters using dialysis bags. (A) Immobilized n-TiO_2 were analyzed by AFM, flat TiO_2 crystals were used as a reference for the roughness effect. (B) Various analytical techniques characterized suspended n-TiO_2.

powder, with a high specific surface area (25–65 m^2/g), is widely used in surface water studies and serves as a reference in toxicological and environmental transformation research [36]. Its strong catalytic and photocatalytic properties make it valuable for various industrial and scientific applications [37]. Further details on the characteristics of these particles are described elsewhere [38].

2.1.2. Crystal-TiO_2

Flat TiO_2 crystal substrates (Purity > 99.99 %, crystal orientation:100, structure: rutile, roughness: < 0.5 nm, size: 5*5*0.5 mm) were purchased from Crystal Substrates, Traverse City, USA. The specification of the crystal can be found elsewhere [39].

2.1.3. Dialysis bags

The specifications of the dialysis bags, as well as the conditioning method, are described elsewhere [40]. Briefly, Biotech Cylindrical Cellulose Ester (CE) Membranes (Float-A-Lyzer®, molecular weight cut off = 100 kDa), purchased from Repligen (California, USA), were soaked in 10 % (v/v) ethanol–water and rinsed with distilled water (DW). The membranes were stored in DW until further usage.

Due to the molecular weight cut-off of the bag (100 kDa), colloidal particles and molecules with very large molecular weight, which can disturb the analysis by aggregating with the investigated particles or attaching to the surface of the glue, are excluded from diffusion into the bag. As a result, only dissolved matter and inorganic ions can reach the nanoparticle surface. This enables us to disentangle the formation of the eco-corona from the aggregation of natural colloids with a bit smaller or similar size than the investigated nanoparticles. This is essential since, in this study, we aim to focus on the sorption layer instead of the hetero-aggregative behavior. Nonetheless, the limit between aggregation and sorption is arbitrary and is here operationally defined as the cut-off of the membrane, which roughly corresponds to half the size of the particles.

The exposure time of the dialysis bags to surface waters was optimized to 48 h in our previous work [33]. This duration is long enough to allow equilibrium of DOM between the inside and outside of the dialysis bags, which typically occurs within a few hours, depending on temperature and water characteristics. At the same time, it is short enough to prevent membrane degradation (both chemical and biological) in river waters. It should be noted that this experimental setup is not

intended to capture the kinetics of sorption, which depend on the initial concentrations and diffusion rate through the membrane. Instead, the study focuses on assessing the final surface state after equilibrium has been reached.

2.1.4. Surface waters and measuring their physicochemical parameters

The three surface water sites as SW1, SW2, and SW3 (Table 1) were selected from a larger dataset obtained in our previous study [33]. All sites are located in Germany. Detailed properties are provided in Tables S2, S3-1, S3-2, and Fig. S1.

Water chemistry measurements followed procedures from our previous work [11]. Samples were collected in HDPE canisters 1 m from the bank, with pH (SG2-FK SevenGo, Mettler Toledo, Schwerzenbach, Switzerland), electrical conductivity (EC) (Consort C863, Turnhout, Belgium), and alkalinity (Hanna Freshwater Alkalinity Colorimeter, Vöhringen, Germany) measured on-site. Samples were transported within 3 h in portable refrigerators, filtered upon arrival using 0.7 μm glass microfiber filters (Labsolute, Germany; calcined at 400 °C for 5 h), then stored in the dark at 4 °C. Dissolved organic matter (DOC) was measured using a TOC analyzer (multi-N/C 2100, Analytik Jena AG, Germany). Anions (F^-, Cl^-, SO_4^{2-}) and cations (Na^+, K^+, Ca^{2+}, Mg^{2+}) were analyzed by ion chromatography (Professional IC 881, Metrohm, Herisau, Switzerland).

The quality of DOC, including its source and chemical composition such as humic substances, fulvic acids, proteins, and aromaticity was evaluated via UV–Vis and fluorescence spectroscopy [41]. UV–Vis spectra were obtained with a Jena-Specord50 spectrophotometer (Analytik Jena, Jena, Germany). Fluorescence excitation/emission matrices (EEMs) were recorded using a PerkinElmer LS 55 (MA, USA), with emission from 250 to 700 nm in 20 nm increments at 1200 nm/min scan rate. Both excitation and emission slit widths were 10 nm. Indices for fluorescence and UV–Vis were calculated with the "Stardom" R package (R-4.1.0) after correcting for the inner filter effect.

2.2. n-TiO_2 (in suspension): Exposure of n-TiO_2 to surface waters using dialysis bags

The exposure of n-TiO_2 to different surface waters using dialysis bags is fully detailed in our previous work [11]. The exposure was performed on the same day (October 2023) and in the same positions (Table S2) of water collection. In brief, the dialysis bags were filled with 10 mL of a 2 g/L suspension of n-TiO_2 (two dialysis bags for each surface water) and exposed to the surface waters for 48 h. After collection, the suspended particles from the two bags were pooled together into a centrifuge tube. The pooled suspensions were centrifuged at 4500 rpm (3283 g) for 60 min. The supernatant was withdrawn carefully to the last drop. The remaining centrifugate was freeze-dried (Christ, Osterode, Germany) for two continuous days at −40 °C and 0.12 mbar. The freeze-dried samples were used for HR-TEM, ζ-potential, ATR-FTIR, XPS, and LDI-FT-ICR MS analyses. The effect of freeze drying on ATR-FTIR and XPS is discussed in SI (SI/ Part1-1). To provide a reference of unexposed, i.e., pristine nanoparticles for each analysis, n-TiO_2 were dialyzed against deionized water (48 h) in the bags to remove the soluble residue from them.

Table 1
Abbreviations used to represent the sample names in this study.

Abbreviation	Sample
SW1	Surface water 1[1]
n-TiO_2	Pristine TiO_2 P25 nanoparticles.
Crystal-TiO_2	Pristine crystal TiO_2 substrate.
n-TiO_2/SW1	n-TiO_2 nanoparticles exposed to the surface water 1[1]
Crystal-TiO_2/SW1	Crystal-TiO_2 Substrate exposed to the surface water 1[1]

[1] The same notation applies for surface waters 2 and 3. All sampling sites are located in Germany. Detailed properties of these surface waters are provided in Tables S2, S3-1, and S3-2.

2.2.1. HR-TEM

Approximately 1 mg of the powder samples were suspended in 1 mL ultrapure water using vortex and ultrasonic bath. A 5 μL drop of this suspension was deposited on a copper TEM-grid coated with a carbon membrane. The excess of liquid was soaked using a filter paper and the remaining water film was left to dry under ambient conditions.

Transmission electron microscopy (TEM) measurements were performed using a JEOL 2100F (JEOL Ltd., Tokyo, Japan) field emission gun instrument operating at 200 kV equipped with a polar piece of ultra-high resolution. Images were recorded on an UltraScan 4000 Gatan (Gatan Inc., Pleasanton, CA, United States) camera with a 4 k × 4 k pixel CCD. ImageJ was used to estimate the size of the nanoparticles.

2.2.2. ζ-potential

The ζ-potential measurements of the nanoparticles have been reported previously by our group [33]. Briefly, 2.2 mL of each surface water was centrifuged at 5,000 rpm (4.050 g) for 60 min (Universal 320, E4123 rotor, Hettich, Switzerland) to obtain a clear supernatant. A 1.5 mL aliquot was transferred into a polystyrene cuvette and mixed with 1.5 μL of nanoparticle suspension (0.5 mg/L, prepared by ultrasonication of 500 mg/L freeze-dried nanoparticles for 30 min). Measurements were performed at 25 °C using a Wallis zeta-potential analyzer (Cordouan Technologies, France) by laser Doppler velocimetry. The ζ-potential was calculated via Smoluchowski's approximation from ten replicates. Calibration with NIST SRM 1993 yielded −56 ± 4 mV, consistent with the certified value (−58 ± 5 mV).

2.2.3. ATR-FTIR

An Agilent Cary 630 FTIR Spectrometer equipped with a single-reflection diamond ATR element was used for ATR-FTIR measurements. Spectra were recorded against an air background before measuring each sample. The spectral resolution was set to 4 cm^{-1}, and 32 scans were averaged for each spectral measurement within the range of 4000–650 cm^{-1}. Two replicates were measured to verify spectral consistency. Peak positions remained unchanged across replicates, and one representative spectrum is reported. Raw spectra were smoothed using a Savitzky-Golay filter (P = 3, n = 21) and visualized with R using the "ggplot2" package.

2.2.4. XPS

The XPS measurements were performed on samples to confirm changes in surface chemistry after exposure, using a K-Alpha + XPS spectrometer (ThermoFisher Scientific, Brno, Czech Republic). The data were acquired and processed using the Thermo Avantage software. All freeze-dried samples were analyzed using a micro-focused, monochromated Al K_α X-ray source (400 μm spot size). The K-Alpha + charge compensation system was employed during analysis, using electrons of 8 eV energy, and low-energy argon ions to prevent any localized charge build-up. Two areas (400 μm each) of the deposited powder were analyzed to confirm reproducibility and homogeneity. One of them is reported for quantitative analysis, as both areas showed comparable results (In case of any discrepancy, a third area would have been measured). The spectra were fitted with one or more Voigt profiles (BE uncertainty: ± 0.2 eV) and use of Shirley background. The full width at half maximum for each peak is comprised between 1.5 and 2 eV, with special care on similar values within one photoelectron line. Scofield sensitivity factors [42] were applied for correction of the peak area and the quantification is given with an error of ± 10 % on the atom concentration. Spectra were referenced on the carbon (C–C, C–H) at 285.0 eV. All spectra were fitted on the same way and same constraints to ensure a confident comparison between the results.

2.2.5. LDI-FT-ICR MS

The LDI-FT-ICR MS analyses were conducted on selected samples to investigate changes in molecular composition following nanoparticle exposure using a 12 T solariX FT-ICR mass spectrometer (Bruker

Daltonics, Bremen, Germany). The instrument was externally calibrated using direct injection of a 2-ppm solution of Suwannee River Fulvic Acid (SRFA) reference material (SRFA-II, 2S101F, International Humic Substances Society). 1 μL of n-TiO_2 suspension, which was exposed to surface water, in addition to an unexposed P25 pristine nanoparticles, was directly deployed on a Stainless-Steel target (384 MTP ground steel, Bruker Daltonics, Bremen, Germany) and left to air dry. All samples were analyzed in negative ion mode using a MALDI source (Smartbeam II), operating at an optimized fluence to minimize fragmentation while ensuring efficient desorption and ionization of the DOM corona. The parameters were as follows: 200 laser shots with a spot size of 20 μm and 20 % laser power were used for each spectrum. A total of 128 spectra were randomly acquired on the target using selective accumulation, resulting in comparable total ion counts (TIC) between spectra (8×10^7–7×10^8). Data acquisition and processing were performed using Bruker Compass Data Analysis software 5.0 (Bruker Daltonics Inc., Billerica, MA, USA). Mass spectra were internally recalibrated with a list of 164 masses (between 247–719.1 m/z) commonly found in SRFA, and calibrant masses with errors > |0.1| ppm were removed, resulting in mass accuracy after linear calibration being better than 0.1 ppm (n = 47). Molecular formulae (MF) were initially assigned to detected peaks using Lambda-Miner [43], based on their exact mass and isotopic distribution. The software was configured with the following elemental constraints for potential formulae: carbon (^{12}C: 1–80,^{13}C: 0–1), hydrogen (^{1}H: 1–198), nitrogen (^{14}N: 0–5, ^{15}N: 0–1), oxygen (^{16}O: 0–40), and sulfur (^{32}S: 0–3, ^{34}S: 0–1). This configuration supported formula validation through an applied isotope filter considering ^{12}C/^{13}C, ^{14}N/^{15}N, and ^{32}S/^{34}S isotopic patterns.

Subsequently, these assigned MFs were further processed and refined in R using more restrictive filtering criteria: elemental counts for nitrogen (N: 0–2) and sulfur (S: 0–1); double bond equivalents (DBE) ranging from 0 to 25; nominal formula mass between 150 and 1000 Da; and DBE normalized by oxygen content (DBE/O) within the range of −10 to 10. Following this filtration, signal intensities were normalized to the sum of all identified mass peak magnitudes of the respective spectrum. These relative peak intensities (RI) are presented in per mill (‰), and an intensity cutoff of 0.05 ‰ was applied. To compare the common MFs with the exposed nanoparticles and the pristine nanoparticle, the relative (percentage) intensity difference (δRI) [44] was calculated for each of the common MFs using the following equation:

$$\delta RI = \frac{RI(prisitne) - RI(exposed)}{RI(prisitne)} \cdot 100\%$$

where:

RI(pristine): RI for an MF of the pristine (unexposed) nanoparticle.

RI(exposed): RI for an MF of a nanoparticle after exposure.

Additional information is provided in the Supporting Information (SI/ Part 1–2).

2.3. AFM

2.3.1. Immobilized n-TiO_2

2.3.1.1. Sample preparation and exposure to surface waters. The AFM sample preparations were conducted under a laminar flow hood to minimize air contamination. Fig. 2 depicts the steps to immobilize n-TiO_2 inside the dialysis bags as follows:

1. A 0.5 cm magnet (FPMYB magnet, China) was placed on a support steel disc.
2. Tempfix® (temperature-sensitive glue) was applied to the magnet. The glue was melted at 120 °C and maintained at this temperature for 5 min to create a homogeneous bubble-free surface, then allowed to cool to room temperature [45].
3. 10 μL of n-TiO_2 suspension (three concentrations: 10, 50, and 100 mg/L) was applied to the glue and allowed to dry at room temperature. At a concentration of 10 mg/L, no detectable particles were observed in the suspension, likely due to insufficient particle density. At 100 mg/L, significant aggregation was evident in the AFM height images, making it impossible to identify single particles (Fig. S2). Single particles were attempted to be isolated to ensure proper adhesion to the glue, as measurements were complicated by aggregation. In contact mode AFM, particles that are loosely immobilized or aggregated may be dislodged during scanning, potentially affecting measurement accuracy. The optimal concentration was 50 mg/L, at which sufficient single particles were visible in the AFM height images.
4. The sample was placed in an oven at 40 °C for 3 h. At this temperature, the glue became sticky but remained solid. After cooling to room temperature, the samples were sonicated for 10 s in a 50 mL beaker containing ultrapure water (18.2 MΩ) placed in an ultrasonic

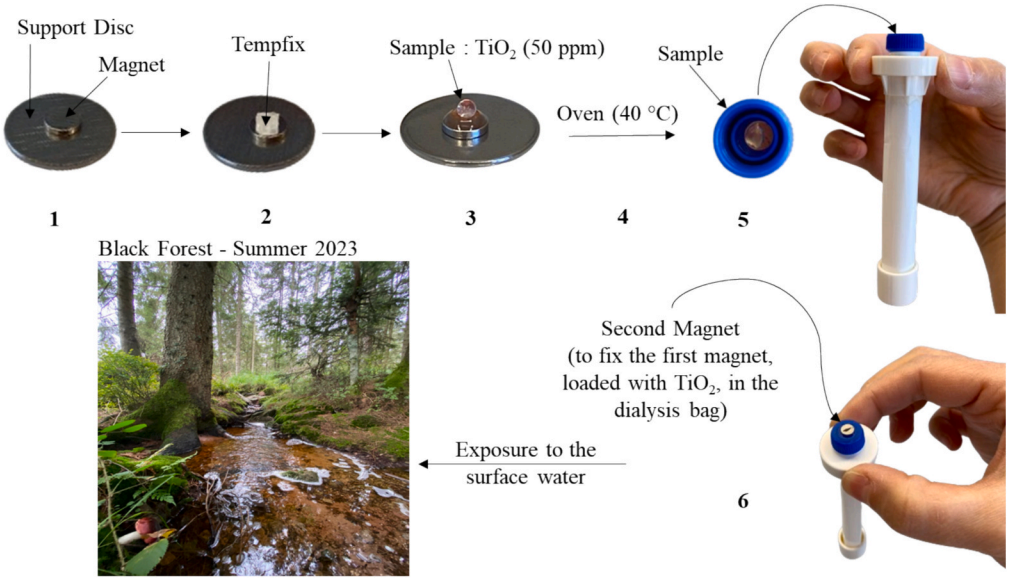

Fig. 2. The schematic steps for immobilizing n-TiO_2 inside the dialysis bags and exposing them to the surface waters (October 2023) before AFM measurements.

bath (12 L, VWR) to remove particles loosely adhered to the adhesive. The samples were rinsed with ultrapure water after sonication.
5. The sample was placed in the cap of the dialysis bag.
6. A second magnet was placed on the outside of the cap to secure the first magnet (loaded with the sample) inside the dialysis bag.

The dialysis bags, with the loaded samples positioned on the cap, were filled with 10 mL of ultrapure water (18.2 MΩ) and placed inside perforated tubes. Two replicates/dialysis bags were prepared for each surface water. The tubes were secured to an anchor and immersed in the surface waters in October 2023. After 48 h, the dialysis bags were retrieved. The water loaded onto the magnet was carefully removed from the cap, down to the last drop, and then dried in a desiccator using silica gel under atmospheric pressure.

2.3.1.2. AFM adhesion force mapping. AFM images were obtained using Peak Force Quantitative Nanomechanical Mapping (PFQNM) mode. The force mapping mode was chosen to enable us to investigate the heterogeneity of the eco-corona at the nanoscale. The small size of the analyzed nanoparticles required a nanometric resolution and, thereafter, a very small tip, hence, excluding approaches using colloidal probe setups or functionalized tips. Furthermore, the mapping mode was needed to obtain many data points for each particle, which was required to characterize the patchiness of the coating.

In this mode, the tip scans across the surface, using a force setpoint of 5 nN (used for all samples), which is maintained by a feedback loop. The surface height at each point is recorded, allowing reconstruction of the topography after the scan is complete. AFM Analyses (Dimension Icon, Bruker Corporation, USA) were conducted with a new sharp silicon tip on a nitride lever (SNL-10). Some critical prerequisites must be addressed when preparing samples and conditions for AFM measurements:

1. Radius of the tip: The AFM tip radius fundamentally determines the lateral resolution of AFM measurements. The larger the radius of the tip and the larger the opening angle of the AFM tip, the greater the enlargement of the lateral dimensions of objects [46]. Hence, to accurately resolve and measure nanoparticles, we used sharp silicon tips (SNL-10, Bruker, USA). The tip radius of the Bruker SNL-10 AFM probe is nominally 2 nm, with a maximum tip radius of up to 12 nm [47]. Hence, it is smaller than the average size of nanoparticles (~25 nm). Under these conditions, the use of functionally modified tips bearing hydrophilic or hydrophobic groups is limited, as such chemical modifications typically increase the effective tip radius beyond the n-TiO_2 dimension, thereby reducing lateral resolution [48].
2. AFM measurements under a nitrogen chamber (nitrogen purity: 99.9992 %): AFM adhesion force measurements of nanoparticles can also be influenced by ambient humidity, known as capillary forces, which arise from the formation of a water meniscus between the tip and the sample due to the thin layer of water that forms on the sample surface under ambient conditions [49]. We minimized these forces by conducting measurements under nitrogen (30 standard cm^3/min) [18]. Hence, the samples were kept under nitrogen for 30 min prior to measurements, maintaining a low relative humidity (RH) of 5.7 %, monitored using a Dostmann Electronic GmbH hygrometer (Wertheim, Germany). At this low RH, capillary forces are significantly reduced; however, residual capillary forces may still be present [50]. Since all measurements were conducted under the same controlled humidity conditions, the adhesion force results remain comparable, and the observed differences can be attributed to the specific properties of each sample.
3. Calibration: Probe calibration was carried out following a methodology similar to that previously reported [45]. Briefly, the deflection sensitivity (S_v) was calibrated on a sapphire disk (Sapphire-12 M, Bruker, Santa Barbara, CA, USA), and the spring constant (k) was determined by the thermal tune method. As an inherent mechanical property of the AFM cantilever, the spring constant remains stable once calibrated, unless the tip sustains damage [51]. To enable comparison of results from exposing n-TiO_2 to different surface waters, the same tip was used for all nanoparticle samples, with spring constant calibration performed only once per tip (a different tip was used for crystal-TiO_2 samples). However, because the tip radius can change during imaging, it was determined separately for each n-TiO_2 sample by scanning a titanium roughness standard (RS-12 M, Bruker) and applying a blind tip reconstruction algorithm to account for alterations in tip geometry.

To quantify the uncertainty associated with the tip radius, two SNL-10 probes were randomly selected. Repeated scans at the same location on the RS-12 M standard using the first tip were performed to assess systematic measurement variability, while scans acquired at different locations of the RS-12 M standard provided an estimate of operator-dependent variation. Measurements obtained with the second tip were then included in the combined analysis, which yielded a relative standard deviation of 6.7 %. This value reflects the tip uncertainty under the specific measurement conditions used in this study. A general estimate of SNL-10 tip-radius uncertainty would require characterization of a larger number of probes.

AFM scans of single particles were acquired under the optimized conditions with a lateral field of view (FOV) smaller than 1 μm (Fig. 3). At this resolution, the scans featured distinct particles with a size of 20–50 nm, in agreement with TEM images of n-TiO_2 [11], while the adhesion forces of the nanoparticles are clearly different from the glue substrates.

The resulting force volume dataset, analyzed with AFM Nanoscope Analysis 2.0 software, combines simultaneously acquired topographic and force information, enabling correlations between mechanical properties and surface features to be explored [52]. For each surface water, 3——4 random locations were selected for image acquisition, with 20——30 nanoparticles imaged in each location. In cases where aggregation was observed, these particles were excluded from further analysis, as aggregation may shift during AFM contact mode measurements and thereby affect the results.

To capture the heterogeneity in adhesion forces across individual nanoparticles, a series of measurements was conducted along an axis traversing each particle. The spacing between adjacent points was chosen to evenly partition the particle diameter, ensuring uniform coverage of the nanoparticle surface. For example, Fig. 3 shows the adhesion forces measured across a single n-TiO_2 with a diameter of 42.8 nm. A total of 214–303 data points was collected per surface water. To compare the samples, each adhesion force was normalized by the specific radius of the used tip [53].

To minimize edge effect, adhesion forces were evaluated exclusively within the central region of each nanoparticle. Accordingly, for adhesion profiles obtained from line scans crossing individual particles, the outermost 10 nm segments at both the beginning and end of each scan were removed using R software. For example, in Fig. 3, the initial and final 10 nm segments of the measurement line were omitted from the dataset. This approach resulted in the exclusion of nanoparticles smaller than 20 nm, leaving between 70 and 146 data points for further analysis. For future studies, increasing the number of replicates is recommended to enhance statistical power and to compensate for the unavoidable exclusion of data from edge regions.

The results were visualized as violin distribution plots using the R packages “ggplot2”, “dplyr”, “car”, “FSA”, and “multcompView”. Since not all data groups satisfied the assumptions of ANOVA (normality and homogeneity of variance), a nonparametric workflow was applied to test for differences between groups [54]. This workflow consisted of a Kruskal-Wallis test to detect overall group effects, followed by Dunn’s post hoc test with Benjamini-Hochberg adjustment for pairwise

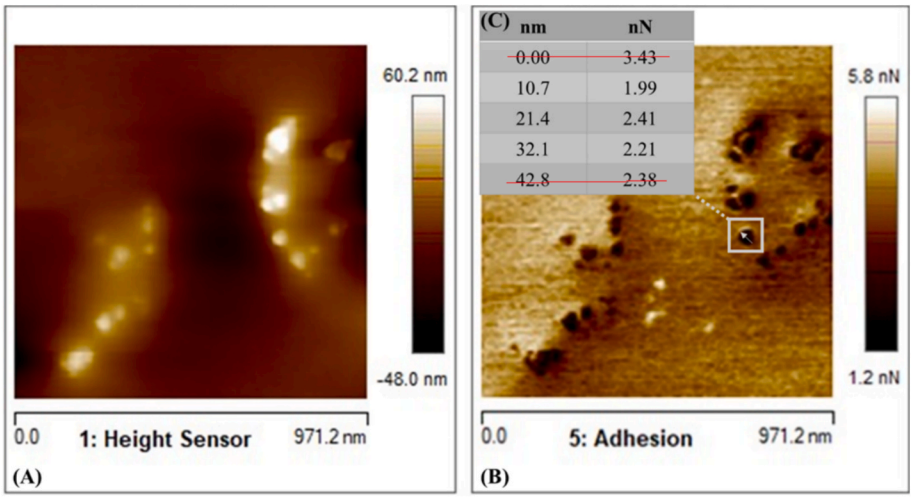

Fig. 3. (A) AFM height and (B) adhesion force images of n-TiO_2 exposed to SW3. (C) Adhesion forces were measured here at intervals of 10.7 nm along an axis traversing a single particle with a diameter of 42.8 nm. The red lines indicate the data segments removed to minimize edge effects during adhesion measurements.

comparisons, and summarizing the pairwise results as a compact letter display (CLD).

2.3.2. *Crystal-TiO_2 substrates*

2.3.2.1. Sample preparation and exposure to surface waters. 50 ml of the water samples collected in part A (October 2023) were centrifuged at 4500 rpm (3283g) for 60 min, and 10 ml of each supernatant was collected for exposure experiments. In the next step, three flat TiO_2 crystal substrates were placed in separate glass petri dishes, followed by the addition of 10 ml of each supernatant. The samples were then placed on a horizontal shaker. After 48 h, the substrates were collected. The residual water on the substrates was carefully removed down to the last drop, and the substrates were dried in a desiccator (filled with silica gel) under atmospheric pressure

2.3.2.2. AFM adhesion force measurement of the crystal-TiO_2 samples. The crystal-TiO_2 substrates were attached to a support disc using double-sided tape (Fig. S3). AFM adhesion force measurements for the TiO_2 substrates, SNL-10 tip was calibrated in the same manner as for the nanoparticles, and the measurements were performed under nitrogen.

In the crystal-TiO_2 experiments, a random region was selected on each crystal surface. Within this region, a set of randomly distributed points (n = 391–1230) was sampled and used to construct the adhesion-force distributions. When natural colloids were observed on the surface in the adhesion map (flat TiO_2 crystal exposed to SW2), those areas were avoided and not selected for further measurements. To determine whether these colloids were organic or inorganic, the samples were heated to 500 °C and maintained at that temperature for 1 h. AFM height images taken after calcination still showed the presence of the colloids, indicating their inorganic nature.

2.3.2.3. Moran's I scatterplot of the crystal-TiO_2 samples. Moran's I scattering was performed to assess the degree and nature of spatial autocorrelation within the data, enabling the identification of spatial clustering, dispersion, and local outliers [55]. Specifically, it helps identify whether the data exhibits clustering, where similar values are spatially grouped, or dispersion, where dissimilar values are neighbors. To visualize the nature and direction of spatial autocorrelation, a Moran scatterplot was generated, in which adhesion values were plotted against their spatially lagged counterparts. The slope of the regression line in this plot corresponds to Moran's I and provides an intuitive representation of the spatial clustering of high or low adhesion values across the sample surface.

Moran's I scattering was performed on the whole scanned area of the crystal-TiO_2 samples and quantified in R using global Moran's I with „spdep" and "gstat" packages. Adhesion values were arranged on a regular x-y grid, and spatial relationships between pixels were defined using a first-order queen contiguity neighborhood [56]. The resulting spatial weights matrix was row-standardized to make the axes more directly comparable [57]. Global Moran's I was calculated, and its significance was evaluated using a Monte-Carlo permutation test to assess the likelihood of obtaining the observed spatial structure under spatial randomness.

2.3.2.4. Water concoct angle. A sessile drop method was used to measure the water contact angle (OCA15Pro, Data Physics, Filderstadt, Germany). A 3 µL drop of ultrapure water was placed manually on the flat TiO_2 crystal substrates (before and after exposure to the surface waters), and an image of the drop was taken after 3 s. The contact angle was then automatically determined by the device. Four drops were measured per sample. The results were plotted using R.

The sessile drop method was selected for this study to ensure methodological consistency with dry-state AFM measurements. Immersion- or submersion-based techniques (Wilhelmy plate, captive bubble) offer advantages such as reduced baseline sensitivity and minimal droplet evaporation but require complete sample wetting, risking dissolution or alteration of soluble eco-corona constituents. Sessile drop measurements are nevertheless subject to droplet evaporation and baseline correction uncertainties. Resulting contact angles should therefore be interpreted cautiously as qualitative indicators of wettability trends rather than precise quantitative surface energy values.

3. Results and discussion

3.1. *Characteristics of the surface waters*

SW1 is an artificial lake surrounded by green areas, with a low DOC concentration of 4.81 mg/L, alkalinity of 124.5 mg/L, and EC of 586.5 µS/cm (Table S3). SW2 is a small stream in a forested, highly calcareous region, exhibiting a similar DOC concentration to SW1 (5.27 mg/L) but with higher alkalinity (322 mg/L as carbonate) and electrical conductivity (1808 µS/cm). In contrast, SW3 drains a peatland and has the highest DOC concentration (40.58 mg/L), the lowest conductivity (41.5 µS/cm), and the lowest alkalinity (2.5 mg/L as carbonate).

Physicochemical properties of the waters are summarized in Table 2 (with detailed data in Tables S3-1 and S3-2). Among the samples, SW3 showed the lowest conductivity and highest DOC (40.58 mg/L).

Table 2
The physicochemical parameters of the waters. EC (electrical conductivity), DOC (dissolved organic carbon), TN (total nitrogen), BIX (biological index), HIX (degree of humification), SR (slope of the absorption spectrum), and SUVA254 (specific ultraviolet absorbance at 254 nm). Comprehensive lists and definitions of water parameters are provided in Tables S2-1 and S2-2.

Name	EC (μS/cm)	Alkalinity (mg/L)	DOC (mg/L)	TN (mg/L)	BIX	HIX	S_R	$SUVA_{254}$
SW1	586.5	124.5	4.81	0.42	0.96	0.72	1.23	3.26
SW2	1808.0	322.0	5.27	0.15	0.55	0.90	0.80	5.87
SW3	41.5	2.5	40.58	0.78	0.32	0.97	0.68	9.40

Additionally, SW3 showed the highest total nitrogen (TN), which represents the sum of all nitrogen forms in the water, including organic nitrogen and inorganic species such as nitrate, nitrite, and ammonium, and is a key indicator of nutrient levels that influence water quality and ecosystem productivity. SW3 also exhibits the highest $SUVA_{254}$ (specific ultraviolet absorbance at 254 nm), and HIX (humification index), alongside lowest S_R (slope ratio) and BIX (biological index) [41,58]. Our previous FT-ICR MS study attributed SW3 the highest O/C and lowest H/C ratios [59], indicating oxygen-rich, high molecular weight aromatic humic substances consistent with its peatland origin.

SW1 and SW2 had similar DOC (~5 mg/L), but SW1 exhibited higher TN, S_R and BIX, and lower $SUVA_{254}$ and HIX compared to SW2, indicating less aromatic and a dominant contribution from recent microbial or algal activity in SW1 [60]. SW2's indices lay between SW1 and SW3 and is distinguished by high alkalinity due to its calcareous catchment.

3.2. *n-TiO_2: Characterization of n-TiO_2 exposed to the surface waters*

3.2.1. *HR-TEM*

HR-TEM analysis of the nanoparticles before and after exposure to surface waters showed no detectable changes in nanoparticle morphology (Fig. 4). The mean nanoparticle size remained nearly constant across all samples at 25.0 ± 0.5 nm (Fig. S4).

3.2.2. *ζ-potential*

The pH of the surrounding environment significantly affects the formation and characteristics of coatings on nanoparticles, including the surface charge. Pristine n–TiO_2 particles exhibit positive ζ-potential at acidic pH, due to the protonation of surface hydroxyl groups, indicating a positively charged nanoparticle surface [11]. The isoelectric point (IEP) of these particles is approximately pH 6.5, where the nanoparticles have zero net surface charge, reflected by a ζ-potential close to zero. As

Table 3
The ζ-potential of n-TiO_2 after exposure to the surface waters [33].

	n-TiO_2/SW1	n-TiO_2/SW2	n-TiO_2/SW3
ζ-potential (mV)	−17.79 ± 1.89 (pH = 7.86)	0.00 ± 4.60 (pH = 7.78)	−46.03 ± 2.83 (pH = 3.70)

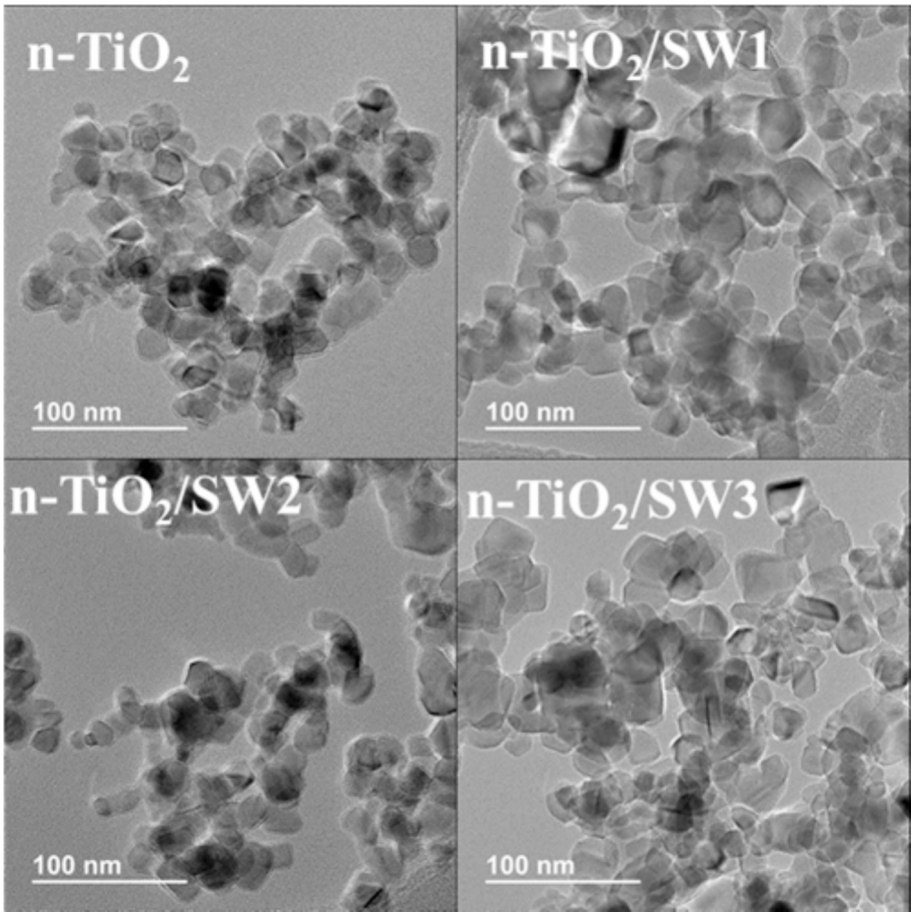

Fig. 4. HR-TEM images of the n-TiO_2 before and after exposure to the surface waters. Size histograms are shown in Fig. S4.

the pH increases beyond this point, the ζ-potential becomes increasingly negative. Table 3 shows the ζ-potential of n-TiO_2 after exposure to different surface waters.

n–TiO_2/SW1 (pH 7.86) shows a zeta potential of −17.79 mV, which aligns with the expected modest negative charge similar to pristine n-TiO_2 under slightly basic conditions. n–TiO_2/SW2 (pH 7.78) exhibits a zeta potential near zero, suggesting that the particles are near their isoelectric point, possibly due to adsorption of DOM or ions from SW2, which can mask or neutralize surface charge. In solutions with high ionic strength like SW2, cations can shield surface charges, diminishing electrostatic repulsion and potentially promoting aggregation despite NOM adsorption [61]. As a result, attractive forces such as van der Waals interactions dominate, leading to a higher likelihood of particle aggregation, which can reduce the available surface area for sorption.

n–TiO_2/SW3 at pH 3.7 exhibits a strongly negative zeta potential (−46.03 mV), demonstrating that the surface coating formed in SW3 reverses the charge from positive (in pristine n-TiO_2) to negative. This charge inversion is attributed to the adsorption of negatively charged DOM and anions, which form an eco–corona that shifts and stabilizes the particle surface charge in the negative range. The eco–corona dominates the intrinsic surface charging behavior of TiO_2, leading to the pronounced negative zeta potential, particularly in natural waters rich in DOM such as SW3. A similar charge reversal upon adsorption of natural organic matter on n-TiO_2 has been reported by Jayalath et. al [62]. At −46.03 mV, there is an electrostatic repulsion between particles, which prevents aggregation and promotes colloidal stability.

It should be noted that the ζ-potential is a measure that explains the surface charge and stability of particles when they are dispersed in a liquid. It provides a useful criterion to compare the eco-corona formation on particles in surface waters. However, it is important to emphasize that ζ-potential values cannot be extrapolated to dried samples, as the measurement and its interpretation are only valid for particles suspended in a liquid medium.

3.2.3. ATR-FTIR

The ATR-FTIR spectra of n-TiO_2 before and after exposure to surface waters are shown in Fig. 5. The band at 1635–1655 cm^{-1} corresponds to Ti-OH bonds [40], which are present in all samples. The appearance of new peaks on n-TiO_2 after exposure to different surface waters results from interactions between the organic and inorganic fractions of the waters and the nanoparticles. These newly observed bands include a broad band at 1380–1400 cm^{-1} (attributed to the symmetric vibration of COO^- in carboxylate groups), a sharp band around 1430 cm^{-1} (corresponding to C=O molecular vibrations in carbonates), and a band near 1510 cm^{-1} (assigned to aromatic C=C stretching) [11]. Notably, n-TiO_2/SW3 depicts a unique band around 1710 cm^{-1}, which is indicative of C=O stretching in carboxylic acids [63]. The band at ~ 1100 cm^{-1} falls within the spectral region characteristic of Si-O stretching vibrations in silica- or silicate-containing materials [64]. Sulfate groups also exhibit S-O stretching modes in this range, contributing to the observed feature in sulfate-bearing systems [65]. Additionally, C-O-C stretching vibrations from polysaccharides and ether-linked organic structures in DOM commonly appear near 1100 cm^{-1}, leading to overlap with these inorganic contributions [66]. The symmetric C-O-C stretching band at 850 cm^{-1} cannot be investigated here due to the presence of overlapping Ti-O bands.

In soil science, hydrophobicity or water repellence of soil organic matter is commonly assessed by analyzing the ratio of C–H (~2983 and 2921 cm^{-1}) to C=O (~1720 cm^{-1}) bonds using IR spectroscopy [67]. This ratio reflects the relative abundance of hydrophobic and hydrophilic functional groups in the soil organic matter. Following this approach, we compared the hydrophilicity of our samples by visually assessing hydrophilic groups (C=O at approximately 1710 cm^{-1}) relative to hydrophobic groups (C–H at approximately 2980 and 2920 cm^{-1}), assuming that the detected signals predominantly represent the surface composition. For n-TiO_2/SW3, a significant increase in hydrophilicity was observed compared to pristine nanoparticles, as indicated by a decrease in the intensity of C–H groups relative to C=O groups (Fig. S5). Other modified samples also exhibited a relative reduction in the intensity of hydrophobic C–H groups compared to pristine nanoparticles. It is important to emphasize that, because the samples were freeze-dried, intensity-based comparisons should be interpreted with caution due to potential alterations introduced by the freeze-drying process (SI/ Part1-1).

Although IR spectra could indicate the presence of functional groups, their identification is often challenging due to overlapping peaks from other groups, and it is further complicated by the fact that IR is a bulk analytical method with limited surface specificity. Hence, as a complementary method, the samples were further investigated by XPS as a surface-sensitive technique.

3.2.4. XPS

The n-TiO_2 composition of the samples was initially confirmed (Table S4) by the ratio of O/Ti~2 in all the samples and the characteristic binding energies observed (Ti 2p with Ti $2p_{3/2}$ at 458.8 eV and O 1 s peak at 530.0 eV). The obtained C 1 s spectrum for pristine n-TiO_2 is fitted into three peaks with different binding energy: the peak at 285.0 eV indicates hydrocarbons (C–H and C–C), the characteristic peak at

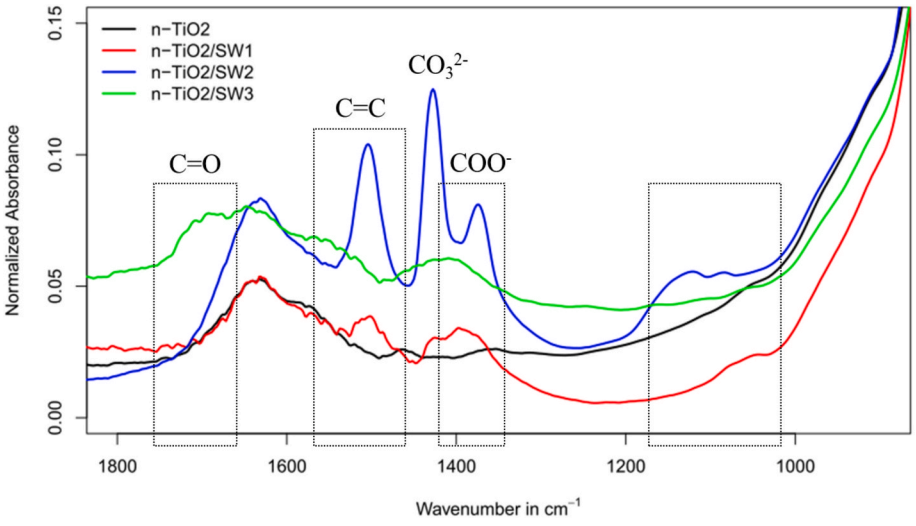

Fig. 5. Representative ATR-FTIR spectra of the n-TiO_2 exposed to SW1, SW2, and SW3. The complete spectra (700–4000 cm^{-1}) are shown in Fig. S5.

286.6 eV relates to alcohol, phenol or ether carbons (C–O), and the peak at 288.8 eV denotes carboxyl carbons (O=C–O) [11]. The presence of these carbon groups on pristine n-TiO_2 is primarily attributed to surface contamination from air [68] or production and storage conditions; hence, the XPS results of exposed samples should be evaluated relative to those of the pristine particles. Table 4 lists the fractional contribution of carbon groups determined by XPS for n-TiO_2 before and after exposure to the surface waters. For meaningful comparison between samples, the atomic percentages of each carbon species (e.g., C–H and C–C) were normalized to the total carbon percentage. This calculation is based on Table S4, providing the carbon concentrations for each chemical environment as well as the concentration in atomic% of all elements present at the surface. XPS survey spectra [69] of the of n-TiO_2 samples is shown in Fig. S6.

The pristine n-TiO_2 exhibited a high fractional contribution of aliphatic carbons (C–H and C–C groups), along with low levels of O=C–O groups, which is consistent with the IR results explaining its higher hydrophobicity compared to the other samples. After exposure of the nanoparticles to surface waters, the ratio of aliphatic carbons to total carbon decreased in all samples, likely due either to the desorption of these molecules upon exposure to surface waters [70], or to the coverage of C–H and C–C groups by newly sorbed carbon–oxygen functional groups.

Notably, n-TiO_2/SW2 is the only sample in which a carbonate coating was detected, indicated by a C 1 s component at 289.5 eV (Table S4). SW2 has a very high alkalinity (322 mg/L), which exceeds the saturation index of $CaCO_3$ [71]. In addition, the 1:1 stoichiometric ratio observed between carbonate (2.1 atomic%) and Ca^{2+} (2.0 atomic %) in n-TiO_2/SW2 suggests the formation of calcium carbonate (calcite) on the nanoparticles [71]. The presence of carbonate in this sample was further confirmed by ATR-FTIR, which shows a sharp band at 1430 cm^{-1} (Fig. 5).

3.2.5. LDI-FT-ICR MS

Further investigation of the samples was carried out using LDI-FT-ICR MS. A comparative analysis of the assigned MFs between the exposed samples and the unexposed pristine n-TiO_2 reveals a notable lack of overlap, suggesting that DOM molecules replaced a large part of the initial coating. Utilizing the calculated δRI, the Van Krevelen (vK) diagrams (Fig. 6) effectively illustrate the common MFs through a color gradient that signifies variations in intensity, thereby reflecting alterations in relative abundance.

Among the samples, n-TiO_2/SW3 displays a distinctive eco-corona pattern characterized by lower hydrogen/carbon (H/C) and higher oxygen/carbon (O/C) ratios compared to n-TiO_2/SW1 and n-TiO_2/SW2. As noted in our earlier research [59], the land use of the area surrounding the surface water influences the type of DOM found in that water. The SW3 contains terrestrial DOM characterized by complex, high molecular weight aromatic compounds (Table S3-2), which are reflected in the eco-corona of the exposed nanoparticles.

Regarding the other two sites, they exhibit comparable low O/C ratios and high H/C ratios of assigned MFs, indicative of similar land use patterns, as both are situated in landscapes where humans have significantly altered the natural vegetation and land cover (Table S2). This environmental context results in the presence of more aliphatic DOM relative to the terrestrial DOM characteristic of SW3. However, n-TiO_2/SW2 demonstrates a higher relative intensity in comparison to n-TiO_2/SW1 across most of the assigned MFs, as illustrated in Fig. 6, where in these vK diagrams the RI is indicated by the dot size and the formula class by color, which correlates with its increased electrical conductivity resulting from high calcium and magnesium ion concentration in this site. This elevated calcium and magnesium ion concentrations facilitate the formation of an aliphatic eco-corona via cation-bridging mechanisms reflecting the nature of present DOM on the nanoparticle surface. Furthermore, n-TiO_2/SW2 exhibits a greater abundance of heteroatomic molecules, specifically MFs containing sulfur (S) and nitrogen (N), where this heteroatomic formula classes constitute 46.56 % of the total assigned MFs, compared to 38.36 % in n-TiO_2/SW1. These observations align with prior findings, indicating that DOM associated with higher concentrations of divalent ions can exhibit an increased prevalence of heteroatomic molecular species [59].

Table 4
XPS results of fractional contributions of each carbon type to total carbon in n-TiO_2/SWs samples. SWs: surface waters. A complete list of atomic percentages of all elements is provided in Table S4.

Photoelectron line	Binding Energy (eV)	n-TiO_2	n-TiO_2/SW1	n-TiO_2/SW2	n-TiO_2/SW3	Assigned species
C1s	285.0	0.90	0.86	0.70	0.76	C–H and C–C
C1s	286.5	0.07	0.06	0.14	0.11	C-O
C1s	288.7	0.03	0.08	0.07	0.12	O=C–O
C1s	289.5	0.00	0.00	0.09	0.00	CO_3^{2-}

3.3. AFM adhesion forces

3.3.1. Flat crystal-TiO_2 substrates: A reference sample for AFM adhesion force measurements

Surface roughness is a critical factor influencing adhesion forces measured by AFM [72]. As roughness increases, the contact area between surfaces becomes more inconsistent, leading to greater fluctuations in measured adhesion forces. This is because rough surfaces have asperities of varying heights and shapes, which respond differently under applied forces, resulting in a broader distribution of adhesion values across different contact points [73]. To systematically investigate the effect of roughness on adhesion, AFM adhesion force measurements were conducted on atomically flat crystal-TiO_2 substrates. These crystal substrates were exposed to the same aqueous environments as the n-TiO_2 to ensure comparable surface interactions.

As P25 n-TiO_2 predominantly exhibits the anatase polymorph (~ 80 % anatase, 20 % rutile), an ideal reference substrate would be a low-roughness anatase single crystal. However, due to the thermodynamic metastability of anatase and the challenges in synthesizing large, low-roughness anatase single crystals, which tend to form nanoscale or porous structures rather than large crystals [74], such substrates are limited in availability. In contrast, the rutile phase is thermodynamically more stable and commercially accessible. Therefore, a rutile single crystal was selected as the reference substrate. Despite the crystallographic differences between anatase and rutile (SI/ Part1-3), both share fundamental TiO_2 chemical characteristics, making rutile a practical and scientifically justified reference for adhesion studies focused on general TiO_2 surface phenomena. It is important to note that, here, we do not compare the adhesion force values of n-TiO_2 and crystal-TiO_2 in terms of their absolute magnitudes. Instead, the analysis focuses on the trends in adhesion forces within each set of measurements.

Fig. 8-left depicts the distribution of adhesion forces measured for crystal-TiO_2 after exposure to surface waters (corresponding 3-D AFM height and adhesion force images are provided in Figs. S8 and S9). For each sample, random data points within the screened region were analyzed (n = 391–1230). The results show an overall increase in adhesion forces after exposure to all three surface waters, with the crystal-TiO_2/SW3 and crystal-TiO_2/SW1 samples exhibiting the largest increases, and crystal-TiO_2/SW2 showing the smallest. Compact letter display (CLD) analysis confirms that these samples differ significantly. Crystal-TiO_2 and crystal-TiO_2/SW2 display a bimodal distribution, indicating the presence of two distinct types of adhesion forces on their surfaces. Moreover, crystal-TiO_2/SW3 shows the highest standard deviation, reflecting the widest range of adhesion forces.

To enable an objective comparison of the samples, the experimental results and relative standard deviations (RSD) of the measured adhesion forces were quantified (Table S5). The mean adhesion force of pristine

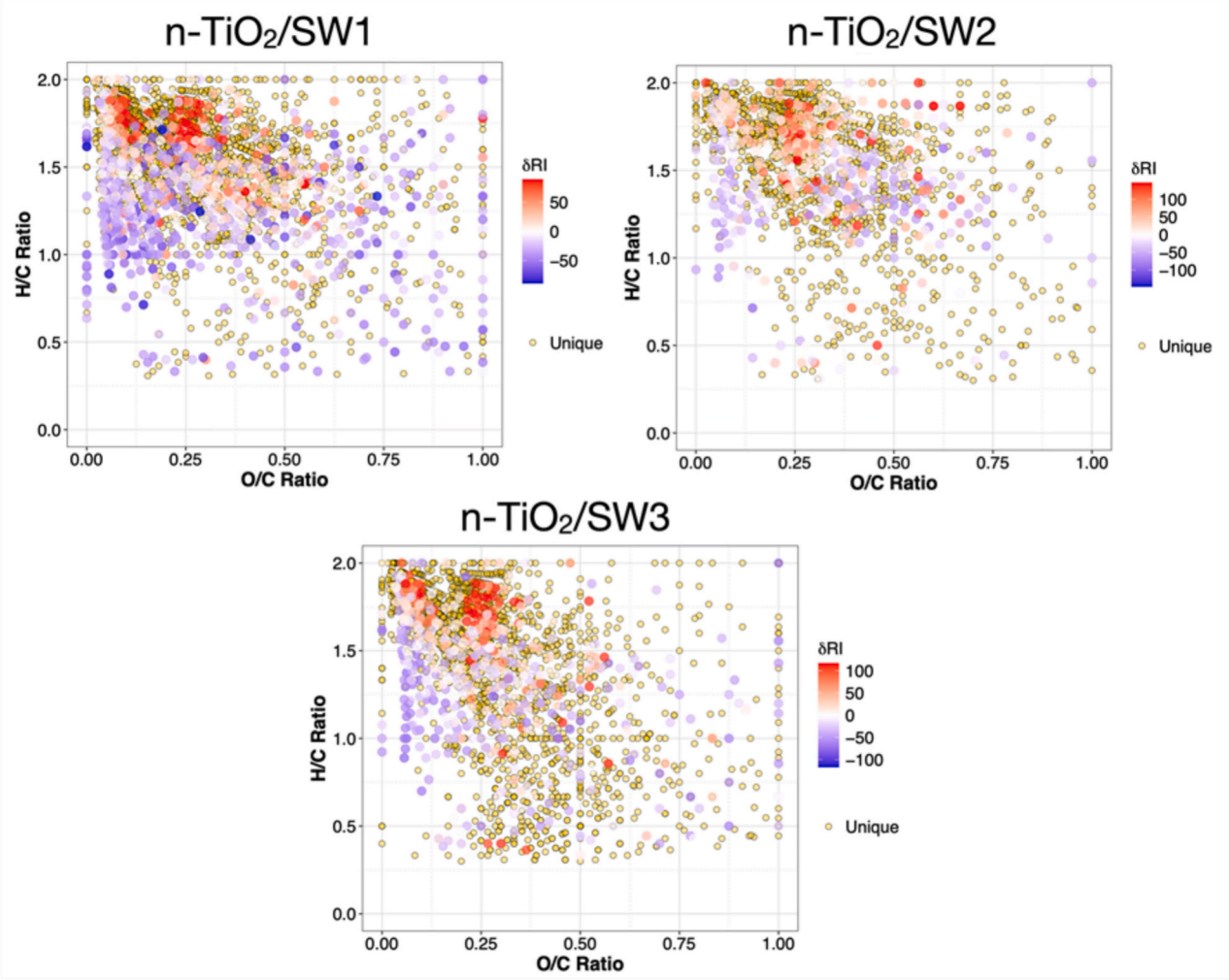

Fig. 6. vK diagrams for n-TiO_2/SWs, demonstrating a color gradient corresponding to the relative intensity difference (δRI) between exposed nanoparticles and pristine nanoparticles. Unique MFs specific to the exposed nanoparticles are indicated as yellow points. Additional information is provided in SI/ Part 1–2-F.

flat crystal-TiO_2, normalized by tip radius, was 0.42 ± 0.02 nN/nm. After exposure to surface waters, all samples exhibited higher adhesion forces relative to the pristine material. The highest adhesion forces were observed for flat crystal-TiO_2/SW3 (1.01 ± 0.1), and TiO_2/SW1 (1.00 ± 0.06), whereas TiO_2/SW2 showed distinctly lower values (0.46 ± 0.04). This pattern suggests that the nature and distribution of functional groups sorbed from SW1 and SW3 promote stronger or more numerous interactions, such as hydrogen bonding, with the AFM tip compared to those formed in SW2. Overall, although exposure to surface waters increases adhesion, the contrasts among SW1, SW3, and SW2 underscore the critical role of surface chemistry and functional group distributions in governing these interactions.

To examine the effect of the number of data points on the adhesion-force distribution, the dataset was expanded to include all data collected over the entire scanned area (n = 4096–16384), as shown in Fig. 8-right. Interestingly, although the mean adhesion forces did not change significantly with the increased number of data points (Table S5), the adhesion-force distribution varied for some samples. For example, the bimodal pattern observed for crystal-TiO_2 (likely due to distinct oxygen and titanium sites [75]) or crystal-TiO_2/SW1 (Fig. 8-left) was no longer evident when data from the entire scanned area were considered (Figs. S8-right). This finding implies patchiness in the samples [76], although adhesion values can vary locally at random positions within the scanned area (bimodal distribution), the overall distribution across the entire scan appears uniform. Crystal-TiO_2/SW3 exhibited a consistently broad unimodal adhesion distribution (RSD ~ 11 %) at both low and full data counts, reflecting diffuse patchiness with continuous force gradients. This important point is discussed in more detail in the following section.

3.3.1.1. Patchiness of the crystal-TiO_2 exposed to the surface waters. Before proceeding, it is important to clearly distinguish between "heterogeneity" and "patchiness" in the context of adhesion force maps in this study. Heterogeneity refers to variability in adhesion forces across the surface [77]; a surface is considered heterogeneous if adhesion values are not uniform, regardless of how those variations are spatially arranged. Patchiness, on the other hand, implies aggregated or clustered distributions, adjacent points or regions exhibit similar adhesion values, and collectively form distinct high-high (high adhesion values surrounded by high-adhesion neighbors) or low-low (low adhesion values surrounded by low-adhesion neighbors) domains. Therefore, a surface can be heterogeneous but not patchy, as in the case of random noise, values fluctuate strongly yet lack spatial organization or contiguous domains.

3.3.1.2. Moran's I scatterplot. The Global Moran's I index (I) quantifies overall spatial autocorrelation across the entire AFM scan, indicating whether adhesion forces exhibit clustering (positive I; patchy), dispersion (negative I), or spatial randomness (I ≈ 0) [78]. Details on interpreting the Moran scatterplot are provided in SI/ Part 1–4. The following

Fig. 7. vK diagrams for n-TiO_2/SWs, illustrating the formula class of each MF represented by a color code. The relative intensity of the MFs is indicated by the size of each dot. n-TiO_2/SW3 is shown in Fig. S7.

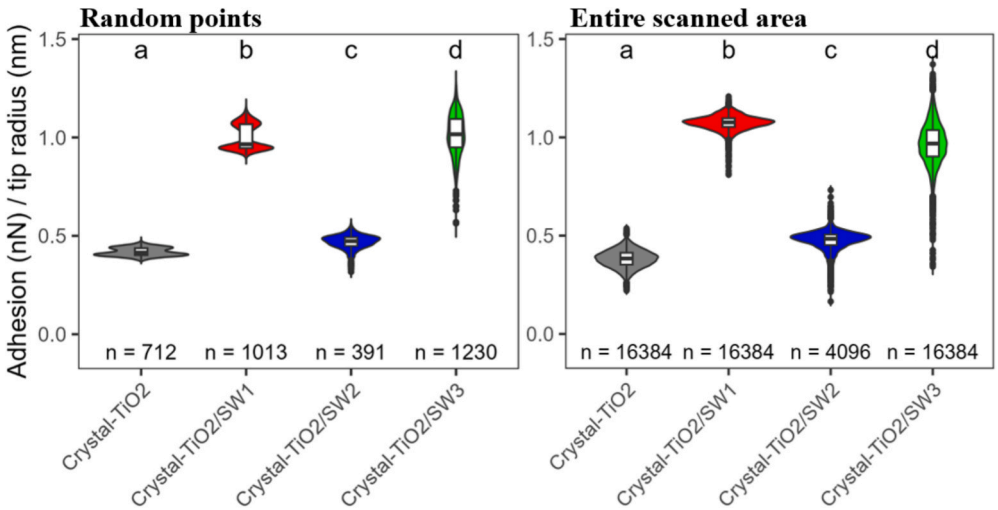

Fig. 8. Violin plots showing the distribution of adhesion forces on crystal-TiO_2 substrates. Left: (random points) selected points within the screened region. Right: entire screened region. n = number of study points.

results characterize nanoparticle-level properties within the scanned area and directly relate to the distribution plots in Fig. 8-right.

Fig. 9 presents the Moran scatterplots for the crystal-TiO_2 samples. All samples show positive Moran's I values, indicating positive spatial autocorrelation [78]. Interestingly, pristine crystal-TiO_2 also exhibits positive Moran's I, likely due to terminal/bridging OH groups that create local variations in adhesion [79], despite near-zero roughness.

Among the samples, crystal-TiO_2/SW3 and crystal-TiO_2/SW1 showed higher Moran's I values than pristine crystal-TiO_2, indicating that sorbed organic matter forms spatially coherent patches rather than random distributions. Crystal-TiO_2/SW3 exhibited the highest Moran's I value (I = 0.57). Its Moran scatterplot shows most adhesion points falling within the High-High (HH) and Low-Low (LL) quadrants, with data points tightly clustered around the regression slope corresponding to Moran's I value. This pattern indicates strong positive spatial autocorrelation, where similar adhesion-force values cluster spatially and reflect pronounced patchiness. This aligns with the polydisperse, heterogeneous nature of humic substances, which adsorb patchily onto mineral surfaces [80].

The Moran scatterplot for crystal-TiO_2/SW1, with a Moran's I value of 0.51, showed positive spatial autocorrelation similar to crystal-TiO_2/SW3, though with slightly less dense clustering around the regression slope. The greater dispersion suggests higher local variability but still reflects significant global spatial organization of adhesion forces. In contrast, the crystal-TiO_2/SW2 scatterplot exhibited the lowest Moran's I value (I = 0.18), even below that of pristine crystal-TiO_2, indicating weakened spatial autocorrelation. Although the positive I value confirms adhesion patchiness, the reduced magnitude reflects lost spatial coherence among neighboring regions. This aligns with inorganic colloids observed on crystal-TiO_2/SW2 surfaces, which disrupt surface

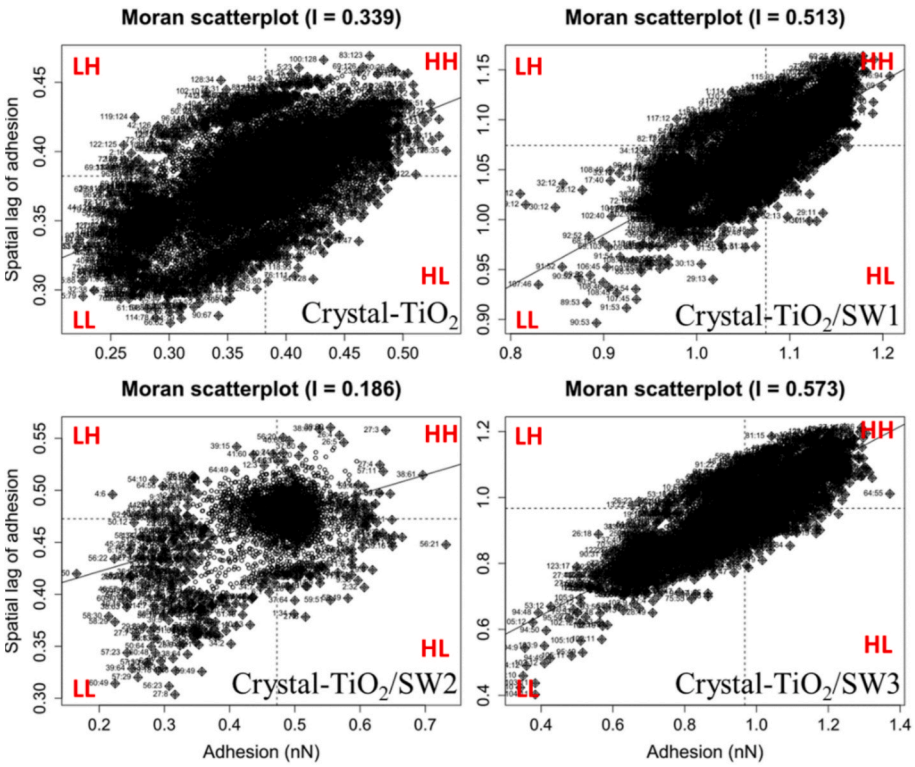

Fig. 9. Moran's I scatterplot. Adhesion forces (x-axis) vs. spatially lagged values (y-axis). Quadrants: HH (high-high), LL (low-low), LH (low–high), and HL (high-low). Slope = Moran's I. Detailed information is provided in SI/ Part 1–4.

continuity and create small, irregularly distributed adhesion sites. Such disordered heterogeneity increases local variability and data dispersion (e.g., cloudy LL outlier cluster), diminishing neighborhood similarity and lowering global Moran's I [81], resulting in a less spatially organized surface compared to pristine crystal-TiO_2.

3.3.1.3. Water contact angle of crystal-TiO_2. The flat TiO_2 crystals were selected to correlate water contact angle measurements with AFM adhesion values because these provide a smooth, chemically uniform, and well-defined surface, minimizing the impact of surface roughness and heterogeneity on the measurements [82]. This ensures that the observed contact angle accurately reflects the intrinsic hydrophilicity determined by surface chemistry, rather than confounding topographical effects [83].

An important point in evaluating contact angle measurements is the intrinsic amphiphilicity of DOM [84], arising from hydrophilic moieties (carboxylates, phenols) alongside hydrophobic components (aliphatic chains, aromatics). Ions further modulate this behavior through charge screening [85], compaction, and bridging [86], yielding eco-coronas with irregular distributions of hydrophobic and hydrophilic groups that preclude straightforward attribution of hydrophilicity to individual functional groups. For example, although Ca^{2+} is a strongly hydrated divalent cation, its presence within an eco-corona does not necessarily produce a uniformly more hydrophilic nanoparticle surface. Calcium ions are not required to reside at the outer corona–water interface but may instead be incorporated within the DOM matrix, for example, by forming cation bridges between adjacent functional groups. Such internal coordination can drive reorganization of the corona architecture and promote the exposure of hydrophobic moieties that were previously shielded from the interface. Hence, the incorporation of Ca^{2+} into the eco-corona and the manifestation of more hydrophobic interfacial characteristics are not mutually exclusive phenomena. Consequently, macroscopic properties such as contact angles and nanoscale features such as AFM adhesion distributions reflect the integrated effects of multiple molecular domains rather than isolated functional groups, manifesting as spatial patchiness and variable interfacial behavior across nanoparticle surfaces.

The pristine TiO_2 substrate showed $\theta = 67°$ (Fig. 10), indicating moderate hydrophilicity ($\theta < 90°$). After surface water exposure, TiO_2/SW1 and TiO_2/SW3 exhibited significantly reduced contact angles, indicating enhanced hydrophilicity. TiO_2/SW3 showed the lowest contact angle, corresponding to the most hydrophilic surface. In contrast, TiO_2/SW2 showed no significant difference in contact angle compared to either the pristine substrate or TiO_2/SW1. The results of flat crystal-TiO_2 exposed to different surface waters, suggest that the composition of surface waters (e.g., organic/inorganic content) differentially modifies TiO_2 surface energies, with SW1 and SW3 increasing hydrophilicity more substantially than SW2.

Comparing water contact angle and AFM adhesion measurements reveals that higher adhesion forces correlate with lower contact angles, indicating increased surface hydrophilicity. The highest AFM adhesion forces were observed for crystal-TiO_2/SW3 (Fig. 8) relative to the other crystal samples, coinciding with the most hydrophilic surface (Fig. 10). This trend suggests that the enhanced adhesion is consistent with an increased contribution of stronger short-range tip-surface interactions, such as dipole–dipole interactions and hydrogen bonding, rather than predominantly weak induced dipole–dipole interactions. Conversely, the lowest adhesion forces were associated with the lowest degree of surface hydrophilicity, indicating that interactions at these surfaces are dominated by weaker, nonpolar dispersive forces.

Notably, the correlation between adhesion forces and contact angle is indeed a simplification, as the two measurements probe different length scales (nanoscale tip-surface contacts versus macroscopic droplet footprints). In our system, however, the surface roughness of all flat crystal-TiO_2 samples is very low and comparable, so roughness-related wetting effects are expected to be similar for all crystals and should not systematically bias the relationship between contact angle and mean adhesion. Consequently, the observed trends predominantly reflect

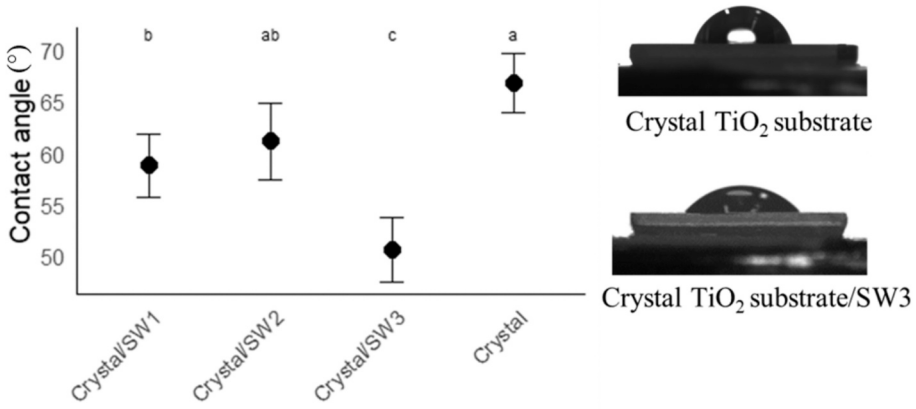

Fig. 10. (Left) water contact angle of flat crystal-TiO_2 substrates before and after exposure to the surface waters (SWs). 4 drops (replicates) were used for each sample. (right) An image of the water contact angle of crystal-TiO_2 substrates before and after exposure to SW3.

differences in surface chemistry and eco-corona structure, while still recognizing that contact angle represents a macroscopic average, whereas AFM adhesion reports on locally heterogeneous nanoscale domains [87].

3.3.2. *Adhesion forces in n-TiO_2*

n-TiO_2 exposed to river waters were analyzed using the same AFM approach as crystal-TiO_2 samples (Fig. S10). Compared to crystal-TiO_2, n-TiO_2 samples exhibit higher variability in adhesion force measurements (Table S5). This variability can be influenced by nanoparticle curvature, which modulates adhesion through changes in the effective contact area (known as the edge effect) [88]. This effect was evident in our results, where higher adhesion forces occur in concave surface regions and lower values in convex regions (Fig. 11) [89]. Additionally, with nanoparticles immobilized on a glue layer, the AFM tip may contact the glue at particle edges, contributing higher adhesion values.

To minimize edge effects in subsequent analyses, nanoparticle edge data points were excluded when calculating adhesion forces. The adhesion force distribution of the n-TiO_2 samples after correction for the edge effect is shown in Fig. 12. This approach yielded a slight to moderate reduction in RSD variability (~ 1 – 20 %; Table S5).

Despite correction for edge effects, all nanoparticle samples still exhibited higher RSDs than the flat crystal-TiO_2 reference (Table S5), indicating greater surface heterogeneity on the nanoparticles. Several factors likely contribute to this behavior. First, the high variability is primarily attributable to surface roughness, which produces non-uniform tip-sample contact; roughness alters the real contact area and the distribution of nanoscale asperities, leading to fluctuations in measured adhesion forces [70]. Second, whereas the crystal-TiO_2 surfaces represent a single rutile crystal face, n-TiO_2 consists of both anatase and rutile phases, each potentially supporting distinct sorption layers, thereby further increasing surface heterogeneity [84]. In addition, uncertainty in the tip radius (RSD = 6.7 %) provides a residual instrumental contribution to the observed variability but remains substantially lower than the RSDs measured for the nanoparticle samples. This indicates that the dominant source of variability arises from nanoscale heterogeneity of the nanoparticle surfaces.

The variation in adhesion force measurements has been previously observed in studies of protein coronas and biofilms. For instance, AFM investigations reveal that biological and molecular heterogeneity, such as local variations in membrane composition, bond formation, and protein corona characteristics, substantially increase adhesion forces and mechanical hysteresis at the nano-bio interface, resulting in heterogeneous adhesion patterns on cell surfaces [90]. Similarly, research on biofilms demonstrates spatial variations in adhesion strength driven by surface morphology and spatial constraints, promotes preferential

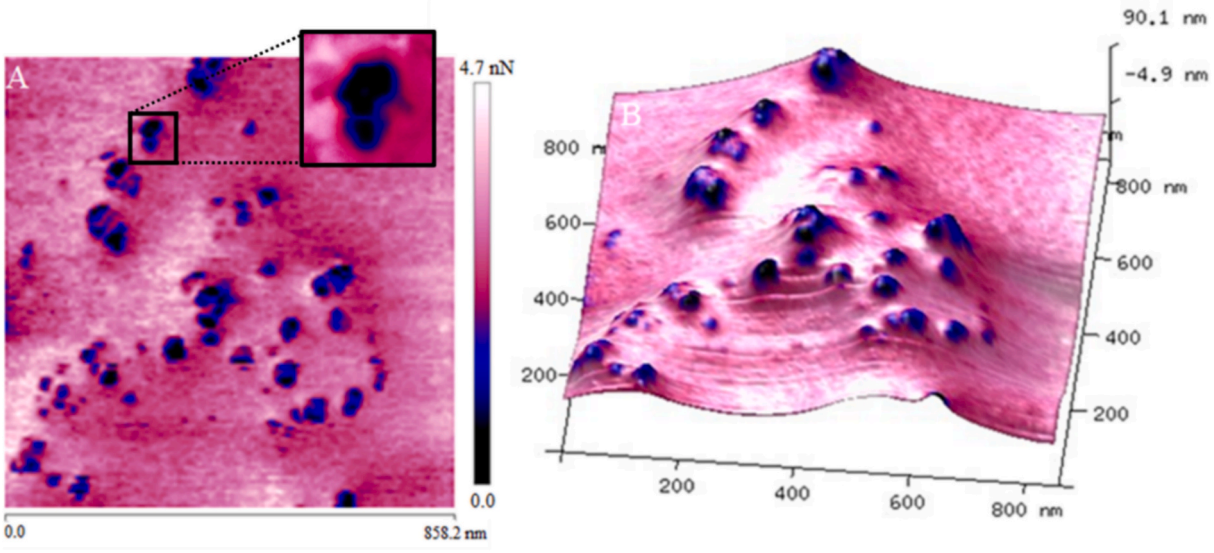

Fig. 11. (Left) 2-D adhesion force, and (right) 3-D height images of n-TiO_2 immobilized onto the glue. Lower adhesion forces are detectable in the center of the nanoparticles (edge effect).

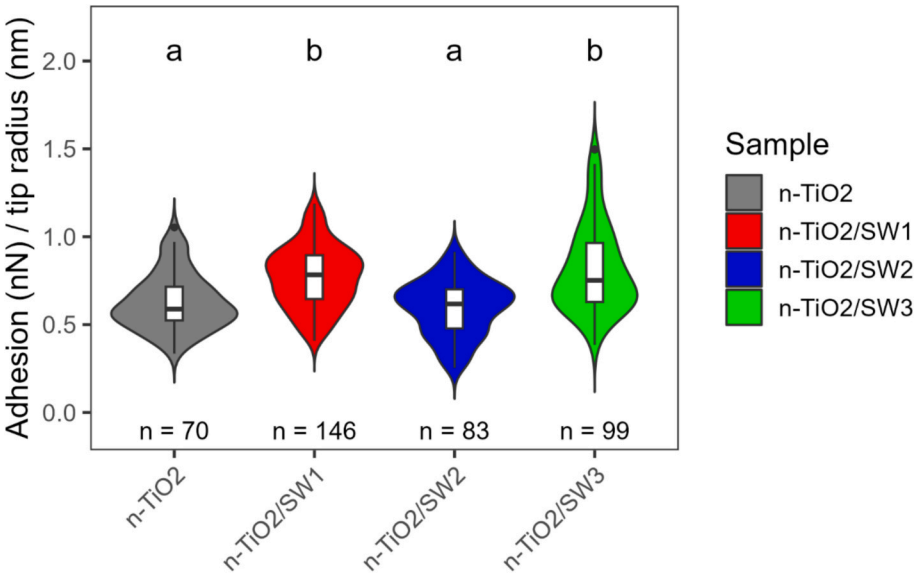

Fig. 12. Violin plots showing the distribution of adhesion forces of the nanoparticles after correction for the edge effect. n = number of study points.

bacterial attachment and enhances spatial heterogeneity [91]. These findings firmly establish that variation in adhesion forces is a characteristic feature of complex biological interfaces.

The cosine similarity between the median responses of crystal-TiO_2 and n-TiO_2 across the four water types was 0.97, indicating an almost identical overall pattern of adhesion changes with water type for both materials [92]. This high similarity shows that, at the level of central tendency, the nanoparticle responses closely track those of the flat crystal reference. In contrast, the compact letter display (CLD) patterns differed markedly between crystals and nanoparticles. For the crystal-TiO_2 samples, each water condition received a different letter, meaning that all four crystal conditions were statistically distinct from one another (Fig. 8). For the nanoparticles (Fig. 12), however, pristine n-TiO_2 and n-TiO_2/SW2 shared one letter group (a), and n-TiO_2/SW1 and n-TiO_2/SW3 shared another (b), meaning these pairs were not significantly different from each other, even though the two letter groups (a and b) themselves were significantly different. This suggests that, despite similar median trends between crystal and nanoparticle systems, the higher variability and heterogeneity in the nanoparticle measurements reduce the ability to resolve individual conditions statistically.

The n-TiO_2 exhibited an average diameter of approximately 25 nm, which imposed significant constraints on single-particle spatial analysis. Because about 20 nm from the particle edges had to be excluded to minimize edge effects, the remaining central region of an individual nanoparticle was insufficient for spatially resolved adhesion mapping suitable for Moran's I scattering analysis. Achieving the required sub-nanometer lateral resolution would necessitate ultra-sharp AFM tips, which were not available in this study. Consequently, Moran's I analysis could not be performed at the single-particle level. However, owing to the high cosine similarity between the surface chemical composition of the nanoparticles and the flat crystal-TiO_2 reference surfaces, the Moran's I result obtained from the crystal surfaces was used as a proxy to evaluate nanoparticle patchiness and to infer how each surface water influenced sorption-related heterogeneity in the next part.

3.4. Discussion of Eco-Corona formation on nanoparticles

3.4.1. n–TiO_2/SW3

The surface water sample SW3, draining a peatland, is characterized by high dissolved organic carbon (DOC: 40.58 mg L^{-1}) and low pH, indicating an acidic environment. The low ionic strength generally favors an expanded conformation of DOM due to weak charge screening; however, acidic conditions promote the protonation of acidic functional groups, reducing the net negative charge and favoring a more folded, compact conformation of DOM [85]. In combination, these factors yield a DOM that is chemically complex and highly humified, as indicated by low S_R and high HIX, consistent with aromatic, high–molecular–weight humic substances typical of peatland origin (Table S3-2). High $SUVA_{254}$ [93] and low BIX further support the dominance of strongly aromatic, terrestrially derived material with limited recent microbial production, while elevated total nitrogen (Table S3-1) corroborate the peatland source.

At acidic pH, pristine n–TiO_2 exhibits positive zeta potentials from surface hydroxyl protonation, but exposure to SW3 promotes formation of a negatively charged eco-corona coating of DOM and anions, inverting the charge to −46.03 mV (Table 3). This strong negative surface charge generates electrostatic repulsion that suppresses aggregation and enhances colloidal stability. ATR-FTIR (Fig. 5) and XPS (Table 4) observations confirmed carboxylic acid functionalities and the distinct surface chemistry of TiO_2/SW3, while LDI reveals lower H/C and higher O/C ratios than other nanoparticles (Fig. 6), reflecting oxygen-rich aromatic humic structures from the peatland source. On this basis, the eco–corona formed in n–TiO_2/SW3 has a complex amphiphilic character, combining hydrophilic and hydrophobic domains. For instance, an increased IR band ratio of C=O to –CH (Fig. S5) and the elevated O/C ratio (Fig. S7) indicate substantial contributions from carboxylic acids and other oxygenated polar groups, which enhance hydrophilicity through hydrogen bonding and strong water affinity [67]. Conversely, the reduced H/C ratio and enriched aromatic content imply hydrophobic regions associated with condensed aromatic structures and other nonpolar moieties, which decrease local water affinity and favor interactions with nonpolar compounds.

In AFM adhesion studies, the largest difference between minimum and maximum adhesion values (adhesion range) for both crystal–TiO_2 and n–TiO_2 was observed for the samples exposed to SW3 (Figs. 8 and 12). This wide adhesion range reflects pronounced heterogenity of the surface coatings under humic-rich conditions, where chemically diverse, polydisperse humic substances adsorb onto TiO_2 in non–uniform fashion and form distinct nanoscale adhesive domains with contrasting properties. In other words, the heterogeneity in the structure of DOM in SW3 can ultimately lead to heterogeneity in the types of groups adsorbed onto nanoparticles [94]. As a result, we expect adhesion maps to exhibit spatially coherent clusters rather than homogeneous coverage. This expectation is confirmed by high global Moran's I values, indicating

positive spatial autocorrelation for crystal-TiO_2/SW3 (Fig. 9). These values demonstrate that adhesion forces form non-random patchy domains rather than distribute randomly across the surface.

TiO_2/SW3 also exhibits higher adhesion forces than pristine TiO_2 for both crystal and nanoparticle samples, indicating stronger tip-surface interactions in the presence of the humic-rich eco–corona. These enhanced forces are consistent with multiple interaction mechanisms, including hydrogen bonding via carboxylic and other polar groups, electrostatic contributions from the strongly negative zeta potential, and hydrophobic interactions involving aromatic domains [95]. The decreased contact angle of crystal–TiO_2/SW3 relative to pristine crystal–TiO_2 indicates increased macroscopic hydrophilicity, probably driven by adsorption of polar, oxygen-containing functionalities (e.g., carboxylic acids [96]) that improve wettability despite the coexistence of hydrophobic aromatic groups.

AFM adhesion force mapping effectively distinguished the SW3 sample from other surface waters by revealing a wider range of adhesion forces (larger min–max differences), higher overall adhesion forces, and pronounced patchiness.

3.4.2. *n–TiO₂/SW2*

SW2 is a small stream situated in a forested, highly calcareous region, characterized by a DOC of 5.27 mg L^{-1} (Table 2), comparable to SW1 but considerably lower than SW3. It shows the highest electrical conductivity (1808 μS cm^{-1}). For instance, the concentration of calcium ions in SW2 is ten times higher than in SW1 (more than 200 times higher than in SW3). The HIX is intermediate, lower than SW3 but higher than SW1; while $SUVA_{254}$ values indicate reduced aromaticity relative to SW3. Total nitrogen concentrations are the lowest among all samples. The elevated ionic strength in SW2 encourages charge shielding by cations, reducing electrostatic repulsion between DOM molecules, which promotes molecular compaction and aggregation despite the presence of natural organic ligands [85].

Surface interactions in n-TiO_2/SW2 show a zeta potential near zero (Table 3) at pH = 7.78, indicating near-complete neutralization of nanoparticle surface charge due to adsorption of ions and DOM in the eco-corona, effectively balancing and screening native charges. XPS analysis (Table S4) reveals elevated aluminum, sulfate, calcium, and uniquely carbonate, consistent with SW2′s calcareous character, indicating extensive ionic complexation neutralizing DOM's negative charge. ATR-FTIR (Fig. 5), and XPS (Table 4) confirm the presence of carbonate. LDI-FT-ICR-MS data (Fig. 6) show the highest hydrogen-to-carbon (H/C) ratio among samples, reflecting dominance of saturated, hydrophobic aliphatic compounds accompanied by significant heteroatom content (N and S). Hence, compared to n-TiO_2/SW3, the n-TiO_2/SW2 eco-corona appears more ionic (inorganic) dominated. The coexistence of ionic or carbonate moieties with hydrophobic aliphatic domains underscores its amphiphilic and compositionally complex nature.

Atomic force microscopy (AFM) adhesion force measurements reveal that n-TiO_2/SW2 exhibits forces comparable to pristine n-TiO_2, lower than two other surface waters. It has been shown that excess Ca^{2+} can bind to carboxylate groups and reduce adhesion forces [97], which may explain the lowest adhesion forces observed in n-TiO_2/SW2. Similarly, crystal-TiO_2/SW2, showed lower adhesion forces than crystal-TiO_2/SW1 and crystal-TiO_2/SW3. Despite Ca^{2+} being a highly hydrated and polar divalent cation, the contact angle of crystal-TiO_2/SW2 remained comparable to pristine crystals, indicating unaltered macroscopic hydrophilicity [98]. This observation likely arises from Ca^{2+}-mediated bridging, which compacts DOM and sequesters polar groups into internal domains, thereby enhancing the relative prominence of hydrophobic moieties on the surface [99].

3.4.3. *n-TiO₂/SW1*

SW1 is an artificial lake surrounded by green areas, characterized by a low DOC of 4.81 mg L^{-1}, pH = 7.86, and an electrical conductivity of 586.5 μS cm^{-1}. This sample exhibits the lowest $SUVA_{254}$ and HIX, together with the highest BIX and S_R (Table 2). A high S_R value is indicative of low molecular-weight [100] and less complex DOM. SW1 with low-molecular-weight substances remains soluble even at high calcium concentrations [101]. Collectively, these optical properties indicate that DOM in SW1 is less aromatic, less humified, and more biologically reactive.

The zeta potential of n-TiO_2/SW1 is slightly negative (Table 3), indicating some adsorption of ions and DOM but without full charge neutralization. XPS analysis (Table 4) reveals the highest normalized C–C/C–H ratio among the samples (Table 4), indicating a greater abundance of aliphatic carbon compared to n-TiO_2/SW2 and n-TiO_2/SW3. LDI-FT-ICR-MS van Krevelen diagram (Fig. 7) reveals a distinct low O/C ratio group absent in n-TiO_2/SW2. Together with the high C–C/C–H signal from XPS, this group is probably attributed to lipid-like compounds. This compositional signature is consistent with waters exhibiting high BIX values and active microbial communities [102].

AFM measurements show that nanoparticles, n-TiO_2/SW1 displays greater adhesion forces than n-TiO_2/SW2 and the pristine n-TiO_2, although the difference from n-TiO_2/SW3 is not statistically significant (Fig. 12). The contact angle of crystal-TiO_2/SW1 was reduced relative to pristine crystal-TiO_2 (Fig. 10), indicating increased macroscopic hydrophilicity. The global Moran's I for crystal-TiO_2/SW1 is positive, indicating spatial autocorrelation and patchiness in the eco-corona coating. The adhesion force range for n-TiO_2/SW1 is narrower than for n-TiO_2/SW3 (Fig. 12), reflecting a narrower force distribution with more uniform adhesion and reduced spatial variability. This pattern likely reflects compositional differences between microbial DOM (SW1) and aromatic-rich terrestrial DOM (SW3) [103], although direct attribution of patchiness variations to molecular-level interactions remains speculative without further structural characterization.

3.4.4. *Limitations of this work*

While this work advances understanding of the eco-corona, several limitations should be noted. The number of environmental replicates was limited to three surface-water samples. This design was not intended to produce a comprehensive mapping of eco-corona variability but to provide a first demonstration that AFM-based adhesion mapping can resolve differences arising from natural DOM compositions. However, broader environmental representation would certainly require inclusion of more sites to identify broader trends and allow for robust statistical analysis. The small size of the nanostructured titanium dioxide particles (~25 nm) also posed constraints, as investigating nanoscale patchiness requires sub-nanometer lateral resolution and ultra-sharp atomic force microscopy (AFM) tips. Consequently, patchiness could only be examined on flat crystal-TiO_2 surfaces rather than individual nanoparticles; this limitation would be less significant for larger particles. Furthermore, controlled laboratory experiments that isolate individual variables are not sufficient because the composition and structure of natural DOM remain insufficiently characterized. In addition, the inherently small field of view in AFM imaging (<1 μm^2) limits the spatial representativeness of the environmental coatings that can be visualized. However, in each sample we analyzed approximately 50–100 individual particles, providing a reasonable basis for assessing coating characteristics. The adhesion and topography data showed consistent patterns across independent images, with no systematic deviations observed between scanned areas. This consistency suggests that the measured regions are representative of the overall sample within the experimental design. While a larger dataset and additional measurement replicates will be required in future studies to capture the full heterogeneity of naturally formed eco-coronas, the present dataset is sufficient to demonstrate methodological feasibility and reliability under the given conditions.

4. Conclusion

This study demonstrates that AFM is a powerful tool for nano-

environmental research. AFM adhesion force mapping enables quantitative assessment of adhesion strength, force range (minimum–maximum differences), and spatial patchiness, thereby resolving nanoscale heterogeneity in environmentally formed nanoparticle coatings. The approach can be applied to investigate nanoparticle coronas at the nanometer scale, providing novel insight into surface heterogeneity that has not been previously achieved, while laying the groundwork for future mechanistic studies on eco-corona formation and transformation.

Nanoparticles exhibited increased adhesion forces in surface waters SW1 and SW3 compared to pristine samples, though high variability arose from surface roughness. Flat crystal-TiO_2 substrates exposed to the same waters served as reference surfaces to evaluate this effect. Moran's I analysis revealed positive spatial autocorrelations across all samples, indicating non-random eco-corona coatings with distinct high- and low-adhesion patches. The variability of the surface, among the samples, was confirmed by complementary ATR-FTIR, XPS, and LDI-FT-ICR MS analyses, which revealed distinct coating chemistries.

These findings highlight eco-corona heterogeneity across aquatic environments and underscore the interplay between particle surface properties and water chemistry in governing nanoparticle behavior. However, the conclusions are derived from three surface waters and thus cannot be broadly generalized, but they demonstrate AFM's utility for characterizing natural eco-coronas. Future work should expand the sample size for greater statistical power and build on this multi-technique approach for comprehensive characterization of nanoparticle-environment interactions.

Declaration of generative AI and AI-assisted technologies in the writing process

At the end of the preparation of the manuscript, the main author used Perplexity.ai to improve the readability and language of the manuscript. After finishing with this service, the author carefully reviewed and edited the content as needed and takes full responsibility for the content of the published article.

CRediT authorship contribution statement

Narjes Tayyebi Sabet Khomami: Writing – review & editing, Writing – original draft, Visualization, Validation, Software, Methodology, Investigation, Formal analysis, Data curation, Conceptualization. **Allan Philippe:** Writing – review & editing, Validation, Supervision, Software, Project administration, Methodology, Conceptualization. **Abd Alaziz Abu Quba:** Writing – review & editing, Validation, Methodology, Investigation, Conceptualization. **Michel Gad:** Writing – review & editing, Validation, Software, Methodology, Investigation, Formal analysis, Data curation. **Oliver Lechtenfeld:** Writing – review & editing, Validation, Supervision, Methodology. **Fintan Hahn:** Writing – review & editing, Investigation. **Vanessa Trouillet:** Writing – review & editing, Investigation. **Jean-Michel Guigner:** Investigation, Writing – review & editing.

Declaration of competing interest

The authors declare the following financial interests/personal relationships which may be considered as potential competing interests: Narjes Tayyebi reports financial support was provided by German Research Foundation. If there are other authors, they declare that they have no known competing financial interests or personal relationships that could have appeared to influence the work reported in this paper.

Acknowledgments

This research was funded by the German Research Foundation, Germany (DFG, project number: 458047880, PH 277/4-1 and LE 3784/8-1). The authors would also like to thank the local authorities and water body owners who authorized us to carry out the field experiment, Karin Meyer for characterizing ion concentrations and DOC, and Mathilde Knott and Gabrielle E. Schaumann for their organizational support as group leaders. We thank Jan Kaesler for supporting LDI-FT-ICR MS measurements and Johann Wurz for software development.

Appendix A. Supplementary material

Supplementary data to this article can be found online at https://doi.org/10.1016/j.apsusc.2026.165927.

Data availability

Data will be made available on request.

References

[1] F. Parrino, L. Palmisano, Titanium dioxide (TiO_2) and its applications, Elsevier, 2020.
[2] R. Daghrir, P. Drogui, D. Robert, Modified TiO2 for environmental photocatalytic applications: a review, Ind. Eng. Chem. Res. 52 (2013) 3581–3599.
[3] M. Janczarek, Ł. Klapiszewski, P. Jędrzejczak, I. Klapiszewska, A. Ślosarczyk, T. Jesionowski, Progress of functionalized TiO_2-based nanomaterials in the construction industry: a comprehensive review, Chem. Eng. J. 430 (2022) 132062.
[4] Nano Titanium Dioxide Narket Forecast, (n.d.). https://www.alliedmarketresearch.com/nano-titanium-dioxide-market (accessed May 2025).
[5] R. Kaegi, A. Englert, A. Gondikas, B. Sinnet, F. von der Kammer, M. Burkhardt, Release of TiO_2-(Nano) particles from construction and demolition landfills, NanoImpact 8 (2017) 73–79.
[6] K. Li, D. Xu, H. Liao, Y. Xue, M. Sun, H. Su, X. Xiu, T. Zhao, A review on the generation, discharge, distribution, environmental behavior, and toxicity (especially to microbial aggregates) of nano-TiO_2 in sewage and surface-water and related research prospects, Sci. Total Environ. 824 (2022) 153866.
[7] Z. Clemente, V. Castro, L. Feitosa, R. Lima, C. Jonsson, A. Maia, L. Fraceto, Fish exposure to nano-TiO_2 under different experimental conditions: methodological aspects for nanoecotoxicology investigations, Sci. Total Environ. 463 (2013) 647–656.
[8] Z. Clemente, V. Castro, C. Jonsson, L. Fraceto, Ecotoxicology of nano-TiO_2-an evaluation of its toxicity to organisms of aquatic ecosystems, (2012).
[9] H. Luo, Y. Xiang, Y. Li, Y. Zhao, X. Pan, Weathering alters surface characteristic of TiO_2-pigmented microplastics and particle size distribution of TiO_2 released into water, Sci. Total Environ. 729 (2020) 139083.
[10] A. Baysal, H. Saygin, G.S. Ustabasi, Physicochemical transformation of ZnO and TiO_2 nanoparticles in sea water and its impact on bacterial toxicity, Environmental Health Engineering and Management, Journal 6 (2019) 73–80.
[11] N.T.S. Khomami, P.M. Patel, C.P. Jusi, V. Trouillet, J. David, G.E. Schaumann, A. Philippe, Influential parameters of surface waters on the formation of coating on TiO_2 nanoparticles under natural conditions, Environ. Sci. Nano 8 (2021) 3153–3166.
[12] M. Auffan, M. Pedeutour, J. Rose, A. Masion, F. Ziarelli, D. Borschneck, C. Chaneac, C. Botta, P. Chaurand, J. Labille, J.-Y. Bottero, Structural degradation at the surface of a TiO(2)-based nanomaterial used in cosmetics, Environ. Sci. Technol. 44 (2010) 2689–2694, https://doi.org/10.1021/es903757q.
[13] J. Bing, X. Xiao, D.J. McClements, Y. Biao, C. Chongjiang, Protein corona formation around inorganic nanoparticles: Food plant proteins-TiO_2 nanoparticle interactions, Food Hydrocoll. 115 (2021) 106594.
[14] T. Du, R. Meng, L. Qian, Z. Wang, T. Li, L. Wu, Formation of extracellular polymeric substances corona on TiO_2 nanoparticles: Roles of crystalline phase and exposed facets, Water Res. 249 (2024) 120990.
[15] B. Yuan, B. Jiang, H. Li, X. Xu, F. Li, D.J. McClements, C. Cao, Interactions between TiO_2 nanoparticles and plant proteins: Role of hydrogen bonding, Food Hydrocoll. 124 (2022) 107302.
[16] S. Darwich, K. Mougin, A. Rao, E. Gnecco, S. Jayaraman, H. Haidara, Manipulation of gold colloidal nanoparticles with atomic force microscopy in dynamic mode: influence of particle-substrate chemistry and morphology, and of operating conditions, Beilstein J. Nanotechnol. 2 (2011) 85–98.
[17] G. Pyrgiotakis, C.O. Blattmann, S. Pratsinis, P. Demokritou, Nanoparticle-nanoparticle interactions in biological media by atomic force microscopy, Langmuir 29 (2013) 11385–11395.
[18] J. Drelich, K.L. Mittal, Atomic Force Microscopy in Adhesion Studies, CRC Press, 2005.
[19] H.-J. Butt, B. Cappella, M. Kappl, Force measurements with the atomic force microscope: technique, interpretation and applications, Surf. Sci. Rep. 59 (2005) 1–152.
[20] Y. Dong, R. An, S. Zhao, W. Cao, L. Huang, W. Zhuang, L. Lu, X. Lu, Molecular interactions of protein with TiO_2 by the AFM-measured adhesion force, Langmuir 33 (2017) 11626–11634.
[21] A.A. Abu Quba, M.-O. Goebel, M. Karagulyan, A. Miltner, M. Kästner, J. Bachmann, G.E. Schaumann, D. Diehl, Hypertonic stress induced changes of

Pseudomonas fluorescens adhesion towards soil minerals studied by AFM, Sci. Rep. 13 (2023) 17146.
[22] C. Aubry, L. Gutierrez, J.P. Croue, Coating of AFM probes with aquatic humic and non-humic NOM to study their adhesion properties, Water Res. 47 (2013) 3109–3119.
[23] S. Oras, S. Vlassov, M. Berholts, R. Lõhmus, K. Mougin, Tuning adhesion forces between functionalized gold colloidal nanoparticles and silicon AFM tips: role of ligands and capillary forces, Beilstein J. Nanotechnol. 9 (2018) 660–670.
[24] R. Huber, S. Stoll, Protein affinity for TiO_2 and CeO_2 manufactured nanoparticles. from ultra-pure water to biological media, Colloids Surf. A: Physicochem. Eng. Asp. (2018).
[25] S. Ghosh, H. Mashayekhi, P. Bhowmik, B. Xing, Colloidal stability of Al2O3 nanoparticles as affected by coating of structurally different humic acids, Langmuir 26 (2009) 873–879.
[26] X. Wang, E. Ma, X. Shen, X. Guo, M. Zhang, H. Zhang, Y. Liu, F. Cai, S. Tao, B. Xing, Effect of model dissolved organic matter coating on sorption of phenanthrene by TiO_2 nanoparticles, Environ. Pollut. 194 (2014) 31–37.
[27] C.-W. Yang, L. Yuan, H.-Z. Zhou, X. Zhang, G.-P. Sheng, Coating ligand-mediated dynamic formation of natural organic matter (NOM) corona on engineered nanoparticles in natural environments, Environ. Sci. Nano 8 (2021) 1029–1041.
[28] S.M. Louie, R.D. Tilton, G.V. Lowry, Critical review: impacts of macromolecular coatings on critical physicochemical processes controlling environmental fate of nanomaterials, Environ. Sci. Nano 3 (2016) 283–310.
[29] J.S. Grant, Z. Zhu, C.R. Anderton, S.K. Shaw, Physical and chemical morphology of passively sampled environmental films, ACS Earth Space Chem. 3 (2019) 305–313.
[30] R. Wang, Y. Li, T. Xiao, L. Cong, Y. Ling, Z. Lu, C. Fukushima, I. Tsuchitori, M. Bazzaoui, Using atomic force microscopy to measure thickness of passive film on stainless steel immersed in aqueous solution, Sci. Rep. 9 (2019) 13094.
[31] K.A. Ramirez-Aguilar, D.W. Lehmpuhl, A.E. Michel, J.W. Birks, K.L. Rowlen, Atomic force microscopy for the analysis of environmental particles, Ultramicroscopy 77 (1999) 187–194.
[32] T. Górecki, J. Namieśnik, Passive sampling, TrAC Trends Anal. Chem. 21 (2002) 276–291.
[33] A. Philippe, N.T.S. Khomami, M. Gad, F. Hahn, V. Trouillet, O. Lechtenfeld, S. Kunz, M.J.G. Aravena, V. Wollersen, E. Di Lodovico, Measuring and predicting the zeta-potential of anthropogenic TiO_2 nanoparticles in surface waters, Environ. Sci. Nano 12 (2025) 4646–4664.
[34] A. Colak, H. Wormeester, H.J. Zandvliet, B. Poelsema, Surface adhesion and its dependence on surface roughness and humidity measured with a flat tip, Appl. Surf. Sci. 258 (2012) 6938–6942.
[35] S.M. Garner, E.A. O'Rear, S.S. Khajotia, F.L.E. Florez, The applicability of a drop penetration method to measure contact angles on TiO_2 and ZnO nanoparticles, Nanomaterials 10 (2020) 1099.
[36] F. Li, Z. Liang, X. Zheng, W. Zhao, M. Wu, Z. Wang, Toxicity of nano-TiO_2 on algae and the site of reactive oxygen species production, Aquat. Toxicol. 158 (2015) 1–13.
[37] L. Mino, C. Negri, R. Santalucia, G. Cerrato, G. Spoto, G. Martra, Morphology, surface structure and water adsorption properties of TiO_2 nanoparticles: a comparison of different commercial samples, Molecules 25 (2020) 4605.
[38] B. Ohtani, O. Prieto-Mahaney, D. Li, R. Abe, What is Degussa (Evonik) P25? Crystalline composition analysis, reconstruction from isolated pure particles and photocatalytic activity test, J. Photochem. Photobiol. A: Chem. 216 (2010) 179–182.
[39] Titanium dioxide, (n.d.). https://www.crystalsubstrates.com/products/titanium-dioxide-tio2-single-crystal-substrate?_pos=1&_sid=9eaaedf4c&_ss=r (accessed February 2025).
[40] N.T.S. Khomami, A. Philippe, O.J. Lechtenfeld, J.M. Guigner, S. Heissler, G. E. Schaumann, Validation of a field deployable reactor for in situ formation of NOM-engineered nanoparticle corona, Environ. Sci. Nano 7 (2020) 486–500.
[41] A. Huguet, L. Vacher, S. Relexans, S. Saubusse, J.-M. Froidefond, E. Parlanti, Properties of fluorescent dissolved organic matter in the Gironde Estuary, Org Geochem. 40 (2009) 706–719.
[42] J.H. Scofield, Hartree-Slater subshell photoionization cross-sections at 1254 and 1487 eV, J. Electron Spectrosc. Relat. Phenom. 8 (1976) 129–137.
[43] J. Wurz, A. Groß, K. Franze, O.J. Lechtenfeld, Lambda-Miner: enhancing reproducible natural organic matter data processing with a semi-automatic web application, EGU Gen. Assembly Conf. Abs. (2024) 15782.
[44] P. Herzsprung, N. Kamjunke, C. Wilske, K. Friese, B. Boehrer, K. Rinke, O. J. Lechtenfeld, W. von Tümpling, Data evaluation strategy for identification of key molecular formulas in dissolved organic matter as proxies for biogeochemical reactivity based on abundance differences from ultrahigh resolution mass spectrometry, Water Res. 232 (2023) 119672.
[45] A.A. Abu Quba, G.E. Schaumann, M. Karagulyan, D. Diehl, et al., A new approach for repeated tip-sample relocation for AFM imaging of nano and micro sized particles and cells in liquid environment, Ultramicroscopy 211 (2020) 112945.
[46] Resolution, (n.d.). https://www.spmtips.com/how-to-choose-afm-probes-by-resolution (accessed May 2025).
[47] brukerafmprobes, (n.d.). https://www.brukerafmprobes.com/p-3693-snl-10.aspx?srsltid=AfmBOor7-EmZMLn_vmwEnj_E8P7ZGeUbPf4rr8s0PGLAxhyYeeCgPnPW (accessed December 2025).
[48] F. Marques-Moros, A. Forment-Aliaga, E. Pinilla-Cienfuegos, J. Canet-Ferrer, Mirror effect in atomic force microscopy profiles enables tip reconstruction, Scientif. Rep. 10 (2020) 18911.
[49] X. Xiao, L. Qian, Investigation of humidity-dependent capillary force, Langmuir 16 (2000) 8153–8158.
[50] A.J. Harrison, D.S. Corti, S.P. Beaudoin, Capillary forces in nanoparticle adhesion: a review of AFM methods, Part. Sci. Technol. 33 (2015) 526–538.
[51] Y. Song, S. Wu, L. Xu, X. Fu, Accurate calibration and uncertainty estimation of the normal spring constant of various AFM cantilevers, Sensors 15 (2015) 5865–5883.
[52] Force Volume Data, (n.d.). https://www.epfl.ch/research/facilities/cmi/wp-content/uploads/2020/03/NanoScopeAnalysisV150Manual.pdf (accessed April 2025).
[53] A.A. Abu Quba, M.-O. Goebel, M. Karagulyan, A. Miltner, M. Kästner, J. Bachmann, G.E. Schaumann, D. Diehl, Changes in cell surface properties of Pseudomonas fluorescens by adaptation to NaCl induced hypertonic stress, FEMS Microbes 4 (2023) xtac028.
[54] H.-P. Piepho, An algorithm for a letter-based representation of all-pairwise comparisons, J. Comput. Graph. Stat. 13 (2004) 456–466.
[55] L. Anselin, Local indicators of spatial association—LISA, Geogr. Anal. 27 (1995) 93–115.
[56] R.S. Bivand, E.J. Pebesma, V. Gomez-Rubio, Applied Spatial Data Analysis with R, Springer, 2008.
[57] E. Pebesma, R. Bivand, Spatial Data Science: with Applications in R, Chapman and Hall/CRC, Boca Raton, 2023, 10.1201/9780429459016.
[58] J. Swietlik, E. Sikorska, Characterization of natural organic matter fractions by high pressure size-exclusion chromatography, specific UV absorbance and total luminescence spectroscopy, Pol. J. Environ. Stud. 15 (2006) 145.
[59] M. Gad, N.T.S. Khomami, R. Krieg, J. Schor, A. Philippe, O.J. Lechtenfeld, Environmental drivers of dissolved organic matter composition across central European aquatic systems: a novel correlation-based machine learning and FT-ICR MS approach, Water Res. 273 (2025) 123018.
[60] J. Zhang, J. Tan, Y. Wang, Spatial differences of dissolved organic matter composition and humification in an artificial Lake, Water Sci. Tech.. 90 (2024) 995–1008.
[61] E.R. CarrawayDr, M.A. Schlautman, The pH dependence of natural organic matter sorption to nanoparticles and its ability to stabilize nanoparticles in aqueous solutions, 27-30 March, Cape Verde. (2014) 64.
[62] S. Jayalath, H. Wu, S.C. Larsen, V.H. Grassian, Surface adsorption of Suwannee River humic acid on TiO_2 nanoparticles: a study of pH and particle size, Langmuir 34 (2018) 3136–3145.
[63] M. Starsinic, Y. Otake, P.L. Walker Jr, P.C. Painter, Application of FT-ir spectroscopy to the determination of COOH groups in coal, Fuel 63 (1984) 1002–1007.
[64] Y. Liang, J. Ouyang, H. Wang, W. Wang, P. Chui, K. Sun, Synthesis and characterization of core-shell structured SiO_2@ YVO_4: Yb^{3+}, Er^{3+} microspheres, Appl. Surf. Sci. 258 (2012) 3689–3694.
[65] D. Peak, R.G. Ford, D.L. Sparks, An in situ ATR-FTIR investigation of sulfate bonding mechanisms on goethite, J. Colloid Interface Sci. 218 (1999) 289–299.
[66] D.L. Pavia, G.M. Lampman, G.S. Kriz, J.R. Vyvyan, Introduction to Spectroscopy (2001).
[67] A.S. Obeng, J. Dunne, M. Giltrap, F. Tian, Soil organic matter carbon chemistry signatures, hydrophobicity and humification index following land use change in temperate peat soils, Heliyon 9 (2023).
[68] Y. Song, B. Zhao, L. Zhang, J. Lü, S. Wang, Y. Dong, J. Hu, The origin of the "snap-in" in the force curve between AFM probe and the water/gas interface of nanobubbles, ChemPhysChem 15 (2014) 492–499.
[69] C.S. Ciobanu, M.V. Predoi, N. Buton, C. Megier, S.L. Iconaru, D. Predoi, Physicochemical characterization of europium-doped hydroxyapatite thin films with antifungal activity, Coatings 12 (2022) 306.
[70] N. Tayyebi Sabet Khomami, A. Welle, S. Kunz, A. Philippe, Sorption of Fulvic acids onto titanium dioxide nanoparticles extracted from commercial sunscreens: ToF-SIMS and high-dimensional data analysis, Coatings 12 (2022) 335.
[71] K. Simkiss, Variations in the crystalline form of calcium carbonate precipitated from artificial sea water, Nature 201 (1964) 492–493.
[72] S.Y. Chae, M.K. Park, S.K. Lee, T.Y. Kim, S.K. Kim, W.I. Lee, Preparation of size-controlled TiO_2 nanoparticles and derivation of optically transparent photocatalytic films, Chem. Mater. 15 (2003) 3326–3331.
[73] S.-H. Kim, P.-K. Choi, Y.-B. Lee, T.-S. Kim, M.-S. Jo, S.-Y. Lee, H.-W. Min, J.-B. Yoon, An experimental and numerical study on adhesion force at the nanoscale, Nanoscale Adv. 6 (2024) 2013–2025.
[74] M. Setvín, B. Daniel, V. Mansfeldova, L. Kavan, P. Scheiber, M. Fidler, M. Schmid, U. Diebold, Surface preparation of TiO_2 anatase (101): pitfalls and how to avoid them, Surf. Sci. 626 (2014) 61–67.
[75] O. Stetsovych, M. Todorovi, T.K. Shimizu, C. Moreno, J.W. Ryan, C.P. Leon, K. Sagisaka, Palomares, Atomic species identification at the (101) anatase surface by simultaneous scanning tunnelling and atomic force microscopy, Nat. Commun. 7265 (2015).
[76] M. Götzinger, W. Peukert, Particle adhesion force distributions on rough surfaces, Langmuir 20 (2004) 5298–5303.
[77] C.H. Ettema, D.A. Wardle, Spatial soil ecology, Trends Ecol. Evol. 17 (2002) 177–183.
[78] E.P. Pinto, M.A. Pires, R.S. Matos, R.R. Zamora, R.P. Menezes, R.S. Araújo, T. M. de Souza, Lacunarity exponent and Moran index: a complementary methodology to analyze AFM images and its application to chitosan films, Physica A 581 (2021) 126192.
[79] L.-M. Liu, P. Crawford, P. Hu, The interaction between adsorbed OH and O_2 on TiO_2 surfaces, Prog. Surf. Sci. 84 (2009) 155–176.
[80] M. Yu, Y. Hua, M.T. Sarwar, H. Yang, Nanoscale interactions of humic acid and minerals reveal mechanisms of carbon protection in soil, Environ. Sci. Technol. 57 (2022) 286–296.

[81] E.S. Thompson, P. Saveyn, M. Declercq, J. Meert, V. Guida, C.D. Eads, E.S. Robles, M.M. Britton, Characterisation of heterogeneity and spatial autocorrelation in phase separating mixtures using Moran's I, J. Colloid Interface Sci. 513 (2018) 180–187.
[82] M. Palencia, Surface free energy of solids by contact angle measurements, J. Sci. Technol. Appl. 2 (2017) 84–93.
[83] X. Huang, I. Gates, Apparent contact angle around the periphery of a liquid drop on roughened surfaces, Sci. Rep. 10 (2020) 8220.
[84] G. Song, R. Mesfioui, A. Dotson, P. Westerhoff, P. Hatcher, Comparison of hydrophobic and amphiphilic fractions of dissolved organic matter from a water reservoir by Fourier transform ion cyclotron resonance mass spectrometry, J. Soil. Sediment. 18 (2018) 1265–1278.
[85] J. Dai, M.F. de Cortalezzi, Influence of pH, ionic strength and natural organic matter concentration on a MIP-Fluorescent sensor for the quantification of DNT in water, Heliyon 5 (2019).
[86] L. Cai, L. Hu, H. Shi, J. Ye, Y. Zhang, H. Kim, Effects of inorganic ions and natural organic matter on the aggregation of nanoplastics, Chemosphere 197 (2018) 142–151.
[87] W. Fu, W. Zhang, Measurement of the surface hydrophobicity of engineered nanoparticles using an atomic force microscope, PCCP 20 (2018) 24434–24443.
[88] H.H. Fang, K.-Y. Chan, L.-C. Xu, Quantification of bacterial adhesion forces using atomic force microscopy (AFM), J. Microbiol. Methods 40 (2000) 89–97.
[89] L. Sirghi, N. Nakagiri, K. Sugisaki, H. Sugimura, O. Takai, Effect of sample topography on adhesive force in atomic force spectroscopy measurements in air, Langmuir 16 (2000) 7796–7800.
[90] Y. Dror, R. Sorkin, G. Brand, O. Boubriak, J. Urban, J. Klein, The effect of the serum corona on interactions between a single nano-object and a living cell, Sci. Rep. 7 (2017) 45758.
[91] R. Millan-Solsona, S.R. Brown, L. Zhang, S.S. Madugula, H. Zhao, B. Dumerer, A. N. Bible, N.V. Lavrik, R.K. Vasudevan, A. Biswas, othersAnalysis of biofilm assembly by large area automated AFM, Npj Biofilms Microbiomes 11 (2025) 75.
[92] M.S.G. Karypis, V. Kumar, M. Steinbach, A comparison of document clustering techniques, in: TextMining Workshop at KDD2000 (May 2000), 2000: pp. 428–439.
[93] J.L. Weishaar, G.R. Aiken, B.A. Bergamaschi, M.S. Fram, R. Fujii, K. Mopper, Evaluation of specific ultraviolet absorbance as an indicator of the chemical composition and reactivity of dissolved organic carbon, Environ. Sci. Technol. 37 (2003) 4702–4708.
[94] G.R. Aiken, H. Hsu-Kim, J.N. Ryan, Influence of dissolved organic matter on the environmental fate of metals, nanoparticles, and colloids, (2011).
[95] M.-K. Lee, Y.-C. Park, Contact angle relaxation and long-lasting hydrophilicity of sputtered anatase TiO_2 thin films by novel quantitative XPS analysis, Langmuir 35 (2019) 2066–2077.
[96] G. Zhou, C. Xu, W. Cheng, Q. Zhang, W. Nie, Effects of oxygen element and oxygen-containing functional groups on surface wettability of coal dust with various metamorphic degrees based on XPS experiment, J. Anal. Methods Chem. 2015 (2015) 467242.
[97] S.L. Eichmann, N.A. Burnham, Calcium-mediated adhesion of nanomaterials in reservoir fluids, Sci. Rep. 7 (2017) 11613.
[98] F. Zhang, Wettability on nanoparticle modified surface: for thermal engineering, 2017.
[99] T. Lin, Z. Lu, W. Chen, Interaction mechanisms of humic acid combined with calcium ions on membrane fouling at different conditions in an ultrafiltration system, Desalination 357 (2015) 26–35.
[100] J.R. Helms, A. Stubbins, J.D. Ritchie, E.C. Minor, D.J. Kieber, K. Mopper, Absorption spectral slopes and slope ratios as indicators of molecular weight, source, and photobleaching of chromophoric dissolved organic matter, Limnol. Oceanogr. 53 (2008) 955–969.
[101] P.F. Römkens, J. Dolfing, Effect of Ca on the solubility and molecular size distribution of DOC and Cu binding in soil solution samples, Environ. Sci. Technol. 32 (1998) 363–369.
[102] P. Glaz, J.-P. Gagné, P. Archambault, P. Sirois, C. Nozais, Impact of forest harvesting on water quality and fluorescence characteristics of dissolved organic matter in eastern Canadian Boreal Shield lakes in summer, Biogeosciences 12 (2015) 6999–7011.
[103] W. Chen, P. Westerhoff, J.A. Leenheer, K. Booksh, Fluorescence excitation-emission matrix regional integration to quantify spectra for dissolved organic matter, Environ. Sci. Technol. 37 (2003) 5701–5710.